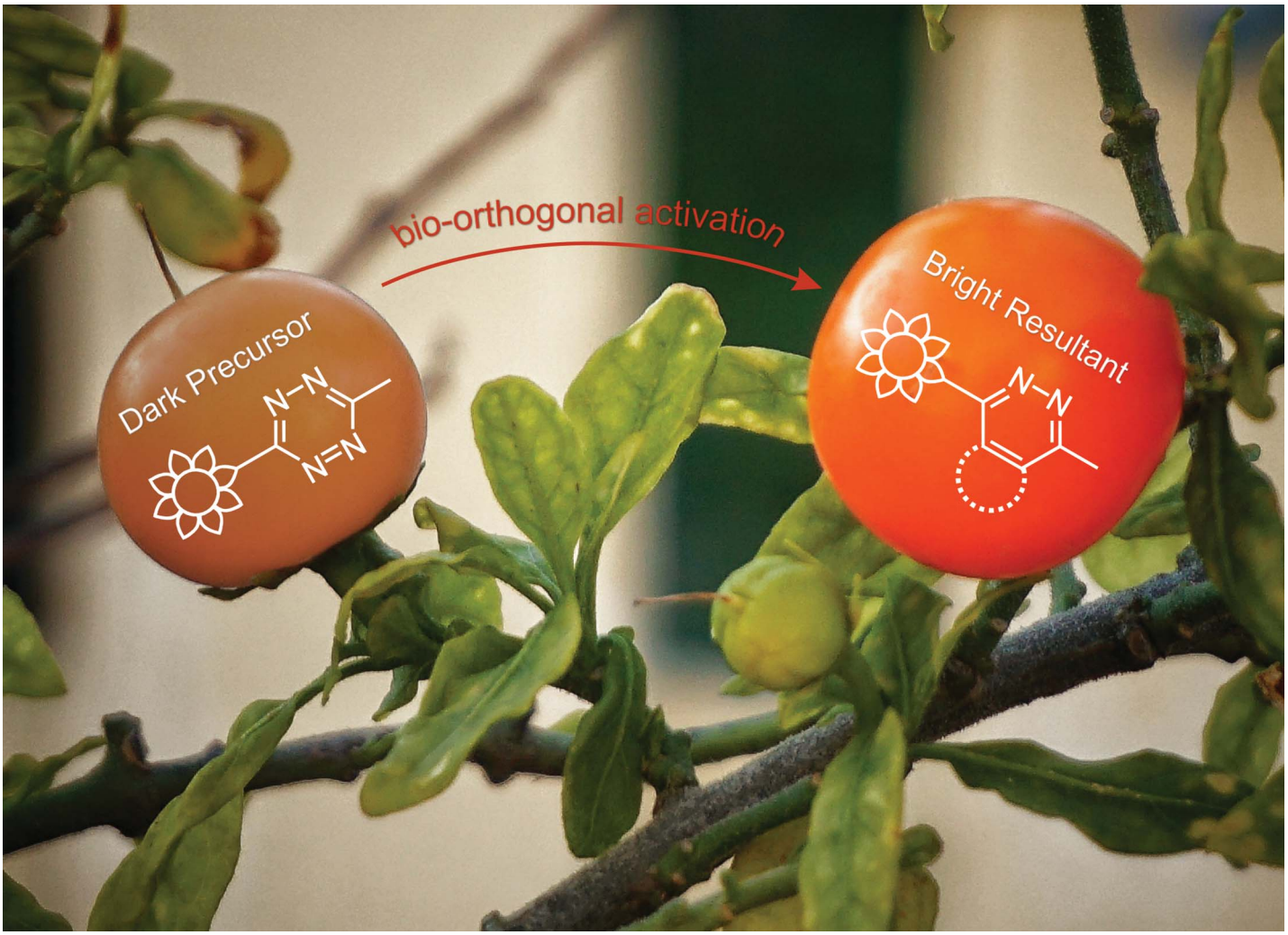

Showcasing research from Tianruo Shen and Xiaogang Liu, Science, Mathematics and Technology Cluster, Singapore University of Technology and Design, Singapore.

Unveiling the photophysical mechanistic mysteries of tetrazine-functionalized fluorogenic labels

This image contrasts a dark, unripe persimmon with a bright, mature one, visually symbolizing the fluorescence recovery of a tetrazine-based fluorogenic label. In bio-orthogonal reactions, the tetrazine fragment undergoes a transformation that restores fluorescence, akin to the persimmon's color change as it ripens.

Image reproduced by permission of Xiaogang Liu from *Chem. Sci.*, 2025, **16**, 4595.

As featured in:

See Tianruo Shen and Xiaogang Liu, *Chem. Sci.*, 2025, **16**, 4595.

ROYAL SOCIETY OF CHEMISTRY

15 YEARS ANNIVERSARY

rsc.li/chemical-science

Registered charity number: 207890

Chemical Science

ROYAL SOCIETY OF CHEMISTRY

REVIEW

View Article Online
View Journal | View Issue

Cite this: *Chem. Sci.*, 2025, **16**, 4595

Unveiling the photophysical mechanistic mysteries of tetrazine-functionalized fluorogenic labels†

Tianruo Shen and Xiaogang Liu *

Tetrazine-based fluorogenic labels are widely utilized in medical and biological studies, exhibiting substantial fluorescence enhancement (FE) following tetrazine degradation through bio-orthogonal reactions. However, the underlying mechanisms driving this fluorogenic response remain only partially resolved, particularly regarding the diminished FE efficiency in the deep-red and near-infrared (NIR) regions. This knowledge gap has impeded efforts to optimize these labels for extended emission wavelengths and improved FE ratios. This review offers a photophysical perspective, discussing the fluorescence quenching pathways (*i.e.*, energy flows and charge separation) that regulate the fluorogenic properties exhibited in various types of tetrazine labels. Moreover, this work examines the emerging role of intramolecular rotations in certain tetrazine-based structures and the integration of additional quencher units. The proposed alternative quenching channel offers the potential to surpass traditional wavelength constraints while achieving improved FE. By examining these photophysical mechanisms, this review aims to advance the understanding of tetrazine-functionalized fluorogenic labels and provide guiding principles for their future design and practical applications.

Received 15th October 2024
Accepted 21st January 2025

DOI: 10.1039/d4sc07018f

rsc.li/chemical-science

1. Introduction

In recent decades, tetrazine-functionalized fluorogenic labels have found widespread utilization in biological and medical contexts.[1–5] This popularity arises from their remarkable chemoselectivity, rapid reaction kinetics, exceptional biocompatibility,

Science, Mathematics and Technology Cluster, Singapore University of Technology and Design, 8 Somapah Road, Singapore 487372, Singapore. E-mail: xiaogang_liu@sutd.edu.sg

† Electronic supplementary information (ESI) available. See DOI: https://doi.org/10.1039/d4sc07018f

Tianruo Shen

Tianruo Shen is a PhD candidate at the Singapore University of Technology and Design (SUTD), under the supervision of Associate Professor Xiaogang Liu. He earned his MEng in Innovation by Design at SUTD in 2021 and continued to pursue his doctoral studies at the same institution, where he applies quantum chemical calculations to facilitate interdisciplinary research. In 2024, he received the "CAS Registry® Innovator" accolade from the Chemical Abstracts Service (CAS) for his contributions to the design of novel chemical molecules. Additionally, for recognizing his outstanding performance in academic excellence and social commitment, he was honored with the "RSC Excellent Student Award" by the Royal Society of Chemistry (RSC) in 2024.

Xiaogang Liu

Xiaogang Liu is an Associate Professor at the Singapore University of Technology and Design (SUTD) and a council member of the Singapore National Institute of Chemistry (SNIC). He obtained his PhD in physics from the University of Cambridge in 2014 under the mentorship of Professor Jacqueline M. Cole. Since joining SUTD in 2017, he has led the Fluorescence Research Group, which focuses on developing functionalized dyes by elucidating structure-property relationships. The research of his team seeks to shift dye chemistry from traditional trial-and-error methods to precise molecular engineering. In recognition of his contributions, he received the "Shimadzu-SNIC Industry Award" in Applied and Translational Chemistry from SNIC in 2022 and was named a "Materials Chemistry Frontiers Emerging Investigator" by RSC in 2023.

and tunable optical properties.[6–11] These attributes make them ideal for diverse employments in living systems, including in bioimaging,[12–16] drug delivery,[17–21] disease diagnosis,[22–24] pathophysiological therapy,[25–30] and hazardous substance detection.[31–33] Notably, bio-orthogonal imaging, leveraging the unique fluorogenicity of these tetrazine labels, stands out among numerous *in vivo* applications. In their native form, these labels are typically non-fluorescent due to the presence of a tetrazine fragment. However, upon tetrazine degradation *via* different bio-orthogonal reactions (Fig. S1, ESI†), such as inverse electron-demand Diels–Alder (iEDDA) reactions with dienophiles,[34–36] [4 + 1] cycloadditions with isocyanides,[37–39] superoxide-responsive triggering,[40] and light-activated tetrazine photo-fragmentation,[41–43] a significant fluorescence enhancement (FE) can be observed. This unique fluorogenic response effectively avoids the requirement for the tedious washing steps and mitigates the interference from the background emissions, thereby increasing both convenience and the signal-to-noise ratio in bio-orthogonal imaging.[44–47] Notably, bio-orthogonal activations with different counterparts result in diverse changes in physical and chemical properties, including reaction kinetics, molar absorption coefficients, ultraviolet-visible (UV-vis) absorption peaks, emission maxima, quantum yields, and FE ratios.[48–51] These variations arise from the distinct products generated during the reactions. Consequently, selecting suitable triggers to degrade tetrazine is critical for optimizing FE ratios and improving other key parameters.

Despite their advantages, persistent challenges restrict the optimization of high-performance tetrazine-derived labels with enhanced fluorogenicity. A primary issue is the undetermined mechanistic basis for their activable photoluminescence effect, particularly the fluorescence quenching that occurs in the precursors before bio-orthogonal reactions. Additionally, extending fluorescence into the deep-red and near-infrared (NIR) regions while maintaining high FE ratios remains challenging. It is, therefore, necessary to understand the photophysical mechanisms that drive the fluorogenicity of these labels for advancing their versatile bio-orthogonal utilizations. This knowledge will be foundational in developing next-generation labels with superior fluorogenic performance.

This review systematically analyzes over a decade of research on tetrazine-based fluorogenic labels from a distinctive standpoint of photophysics (Scheme 1). Section 2 categorizes these labels according to their linking modes and emission wavelengths, offering a foundation for the detailed analysis. Sections 3 and 4 highlight the photophysical mechanisms governing

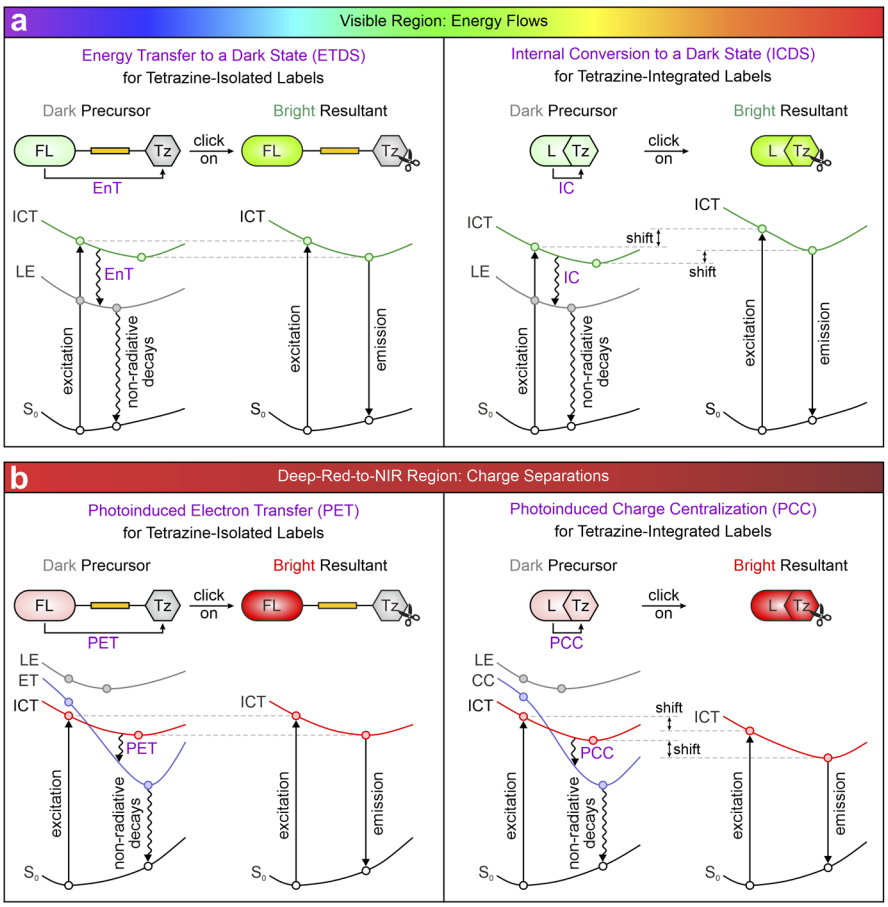

Scheme 1 Illustration of four fluorescence working mechanisms in tetrazine labels across (a) visible and (b) deep-red-to-NIR spectral regions. FL – fluorophore; Tz – tetrazine; L – entire label (FL and Tz share a unified π-conjugation network); S_0 – ground state; ICT – intramolecular charge transfer; LE – locally excited; EnT – energy transfer; IC – internal conversion; ET – electron transfer; CC – charge centralization; PET – photoinduced electron transfer; PCC – photoinduced charge centralization.

their fluorogenic properties across the visible and deep-red-to-NIR spectra. In the visible range, fluorescence quenching in precursors is mainly induced by energy flows (Scheme 1a), *i.e.*, energy transfer (EnT) and internal conversion (IC).[52,53] As emission wavelengths extend into deep-red and NIR regions, charge separation (Scheme 1b), including photoinduced electron transfer (PET) and photoinduced charge centralization (PCC),[54,55] predominates fluorescence quenching. The effectiveness and limitations of these mechanisms are subsequently analyzed by considering various factors affecting these photophysical processes and their fluorogenic behaviors. Section 5 brings focus to two emerging phenomena associated with (dis) aggregation: the "Matthew effect" and torsion-induced disaggregation (TIDA),[56,57] providing unique opportunities for label development through the modulation of aggregation–disaggregation processes. Section 6 explores how the intramolecular motions, *e.g.*, twisted intramolecular charge transfer (TICT), introduce additional quenching channels that deactivate the NIR fluorescence of flexible tetrazine labels. Incorporating additional quenchers for NIR dyes to modulate their fluorescence intensities is also proposed as a future direction. These strategies hold the potential to transcend the traditional wavelength dependence of these labels, henceforward broadening their bio-orthogonal imaging applicability in the NIR range.

2. Classification of tetrazine labels

Tetrazine labels are generally categorized based on the connection mode between the tetrazine fragment and the main fluorophore, specifically whether the two maintain continuous π-conjugation (Scheme 2). The most prevalent arrangement involves linking the former to the latter through non-conjugated spacers with varying lengths, effectively isolating their conjugation systems (Scheme 2a). The non-conjugated linking bridge spatially separates tetrazine and the main fluorophore, allowing each to retain its electronic properties. Upon tetrazine degradation, the fluorescence of the main fluorophore is greatly restored. For instance, Weissleder and co-workers developed a series of tetrazine-isolated labels by attaching tetrazine fragments to various fluorescent derivatives, including boron-dipyrromethene (BODIPY), coumarin, and fluorescein, *via* long non-conjugated linkers (Scheme 2a left).[58] The bio-orthogonal activation of these labels *via* *trans*-cyclooctenol (TCO-OH) effectively restored their fluorescence, yielding emission peaks between 480 and 573 nm and FE ratios from 3.3 to 20.6-fold. In another study, Weissleder *et al.* reduced the linker length by attaching a tetrazine moiety to a BODIPY derivative *via* an orthogonal phenyl ring (Scheme 2a middle),[59] achieving a 1600-fold FE ratio upon bio-orthogonal reactions with TCO-OH. Besides, Wombacher and co-workers engineered a series of rhodamine–tetrazine labels displaying a "face-to-face" configuration (Scheme 2a right), effectively minimizing the distance between the rhodamine and tetrazine units. This design maximizes the quenching effect and enables efficient fluorescence recovery upon bio-orthogonal reactions.[60]

Alternatively, recent studies have introduced another way to incorporate tetrazine into the main fluorophore, using either a single bond or a conjugated linker (*i.e.*, alternating single and double bonds; Scheme 2b). Besides, tetrazine can also be directly incorporated into the backbone of the fluorophore, allowing it to become a fully integrated component with continuous π-conjugation. Such a molecule exhibits high

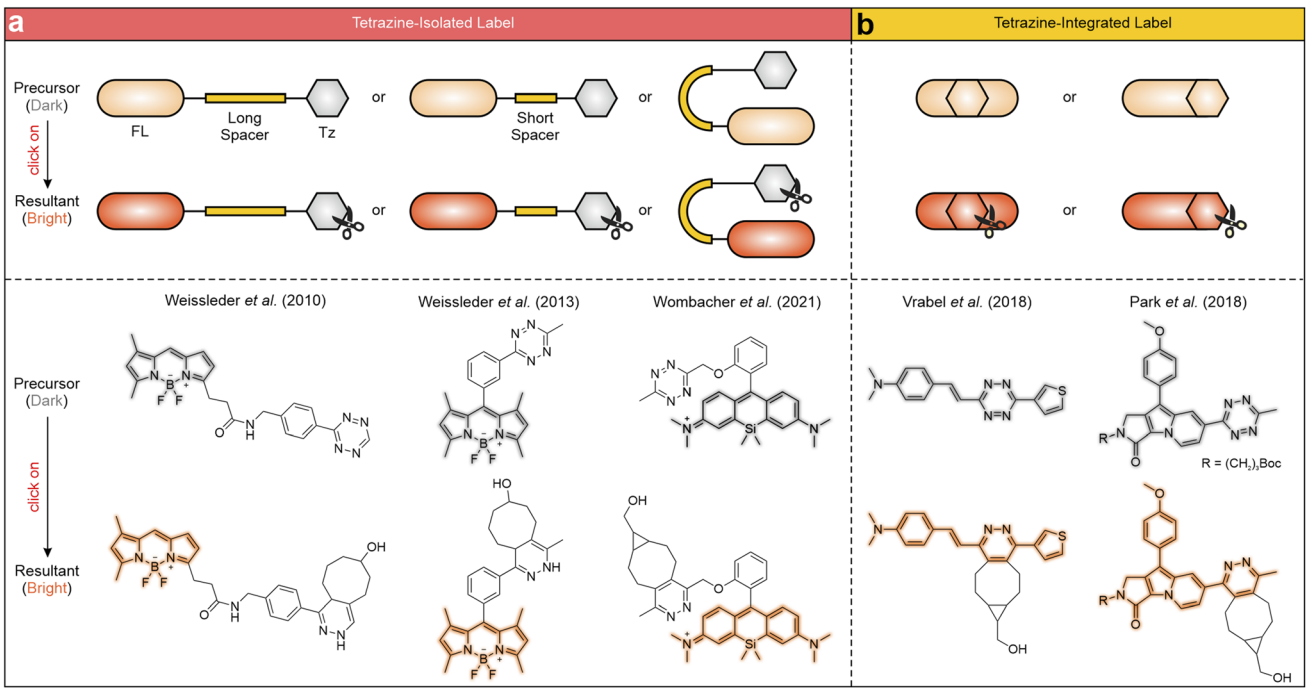

Scheme 2 General features (top) and representative structures (bottom) of (a) tetrazine-isolated and (b) tetrazine-integrated labels before and after iEDDA reactions with TCO-OH or bicyclononyne (BCN). FL – fluorophore; Tz – tetrazine.

planarity, characterized by a small dihedral angle between tetrazine and the main fluorophore. This structural arrangement endows seamless fusion of the tetrazine's conjugation with that of the main fluorophore, facilitating their electronic interactions. After the bio-orthogonal reactions, fluorescence is emitted from the entire label, involving the residual tetrazine component. For example, the group of Vrabel grafted different substituents onto the 3-position and 6-position of tetrazine, creating various conjugation-fused tetrazine-integrated labels (Scheme 2b left).[61–65] The entire labels emitted multiple color fluorescence upon the iEDDA reactions with different dienophiles, as tetrazine moieties (in precursors) and their residues (in resultants) have non-negligible contributions to the π-conjugations of the labels. Park and co-workers further explored monochromophoric tetrazine-fused labels by directly attaching tetrazine fragments to various SF fluorophores (Scheme 2b right).[66]

The development of tetrazine-derived fluorogenic labels has progressed into the deep-red and NIR regions, enhancing their suitability, *e.g.*, reduced phototoxicity, minimized autofluorescence interference, increased tissue penetration, and improved biocompatibility, for bio-orthogonal imaging applications. Consequently, the peak emission wavelength (λ_{em}) has emerged as an additional criterion for classifying these labels on another scale.

Although these labels generally exhibit strong FE ratios post-bio-orthogonal reactions (with reduced FE in the NIR region), the fluorescence quenching mechanisms in the pre-reacted states vary distinctly. These mechanisms under different categories are detailed and discussed in Sections 3 and 4.

3. Energy flows drive the fluorogenicity in tetrazine labels within the visible spectrum

3.1 Energy transfer to a dark state (ETDS) in tetrazine-isolated labels

It is well established that connecting tetrazine to various fluorescent dyes *via* different spacers effectively quenches fluorescence. As depicted in Fig. 1, this quenching phenomenon has been described across a diverse range of conventional dye structures, including BODIPY (**1-1a**, **1-3c**, **1-2a–c**, **1-8a,b**, and **1-5c,d**),[58,59,67–70] fluorescein (**1-1b**, **1-3a**, **1-6a–d**),[47,58,67,71] rhodamine (**1-3b**, **1-5a** and **1-11a–c**),[60,67,72] coumarin (**1-4-d** and **1-10a–d**),[73,74] naphthalene (**1-9a–d**),[75] naphthalimide (**1-12a–d**),[76] cyanine (**1-13a–b**),[77] and nitrobenzoxadiazole (NBD; **1-15a,b**).[69] It also extends to specially synthesized chromophores like Seoul-Fluor (SF; **1-7a–c**) and carbon-dipyrromethene (C-DIPY; **1-14a**).[66,78] Together, these dyes cover a wide range of the visible spectrum, making tetrazine-based quenching applicable to diverse fluorophore families (Fig. 1).

The low background emissions in precursors are mostly considered quenching by energy transfer (EnT). In a visible tetrazine-isolated label, the main fluorophore serves as an energy donor, whereas the tetrazine functionalizes as an energy acceptor. Energy absorbed by the main fluorophore is transferred to the tetrazine through EnT, dissipating its fluorescence *via* non-radiative decays. Choi *et al.* summarized that the EnT processes observed in tetrazine-isolated labels can be classified into three types:[79] Förster resonance EnT (FRET),[80] Dexter EnT (DET),[81] and through-bond EnT (TBET).[82] FRET occurs when the excited-state donor (main fluorophore) transfers energy to the ground-state acceptor (tetrazine) *via* dipole–dipole coupling interactions. This process requires significant overlap between the fluorophore's emission spectrum and tetrazine's absorption spectrum, along with matched transition dipole moments. The FRET efficiency is highly sensitive to the donor–acceptor distance, following an inverse sixth power dependency. It often takes place when the donor–acceptor separation is from 10–100 Å (1–10 nm). In comparison, DET requires direct electronic interactions, which necessitate close spatial proximity and orbital overlap between the fluorophore and tetrazine, typically requiring distances below 10 Å (1 nm). It is worth noting that in FRET/DET-type labels, tetrazine is often linked through a non-conjugated and flexible bridge. The inherent flexibility of these non-conjugated bridges allows the resulting labels to adopt multiple configurations, featuring various distances between the fluorophore and tetrazine. Consequently, the same label could exhibit both FRET and DET quenching processes, depending on the configurations. Conversely, a TBET-type label utilizes a rigid conjugated spacer to connect the main fluorophore to tetrazine with an orthogonal configuration, enhancing the EnT efficiency dramatically.[83] Currently, distinguishing TBET from FRET or DET experimentally remains challenging, as TBET likely represents a specialized form of EnT (including both FRET and DET) facilitated by the rigid conjugated bridges.

To streamline the photophysical models for visible tetrazine-isolated labels, Liu and co-workers proposed a unified fluorescence quenching mechanism, *i.e.*, energy transfer to a dark state (ETDS), emphasizing the inherent non-radiative nature of tetrazine. Taking **1-7b′** (a simplified version of **1-7b** with a methyl substitution; Fig. 2a) as a representative, they demonstrated how a long linker isolates tetrazine from the main fluorophore, preserving the independence of their conjugated systems.[53] This molecule delineates two contrasting states induced by the two independent conjugations. The computational results revealed that during vertical excitation, the main fluorophore, *i.e.*, the SF part, introduces a bright state with a strong oscillator strength ($f = 0.427$; Fig. 2b left), dominating the light absorption upon photoexcitation. This bright π–π* transition state demonstrates a substantial intramolecular charge transfer (ICT) feature with a significant charge transfer distance ($d_{CT} = 1.604$ Å; Fig. 2c left). Below this bright state, a locally excited (LE) state ($d_{CT} = 0.012$ Å) emerges as a dark one ($f = 0.005$), arising from the tetrazine-centred n–π* transition. Following excited-state geometric relaxation, the energy of this dark state stabilizes at 2.097 eV, lying 1.046 eV below that of the bright one. The negligible overlap in hole–electron distributions between the SF and tetrazine fragments further characterizes **1-7b′** as a dual-conjugation system, with two electronically independent π-systems. Consequently, EnT from the SF fragment (energy donor) to tetrazine (energy acceptor) effectively quenches the

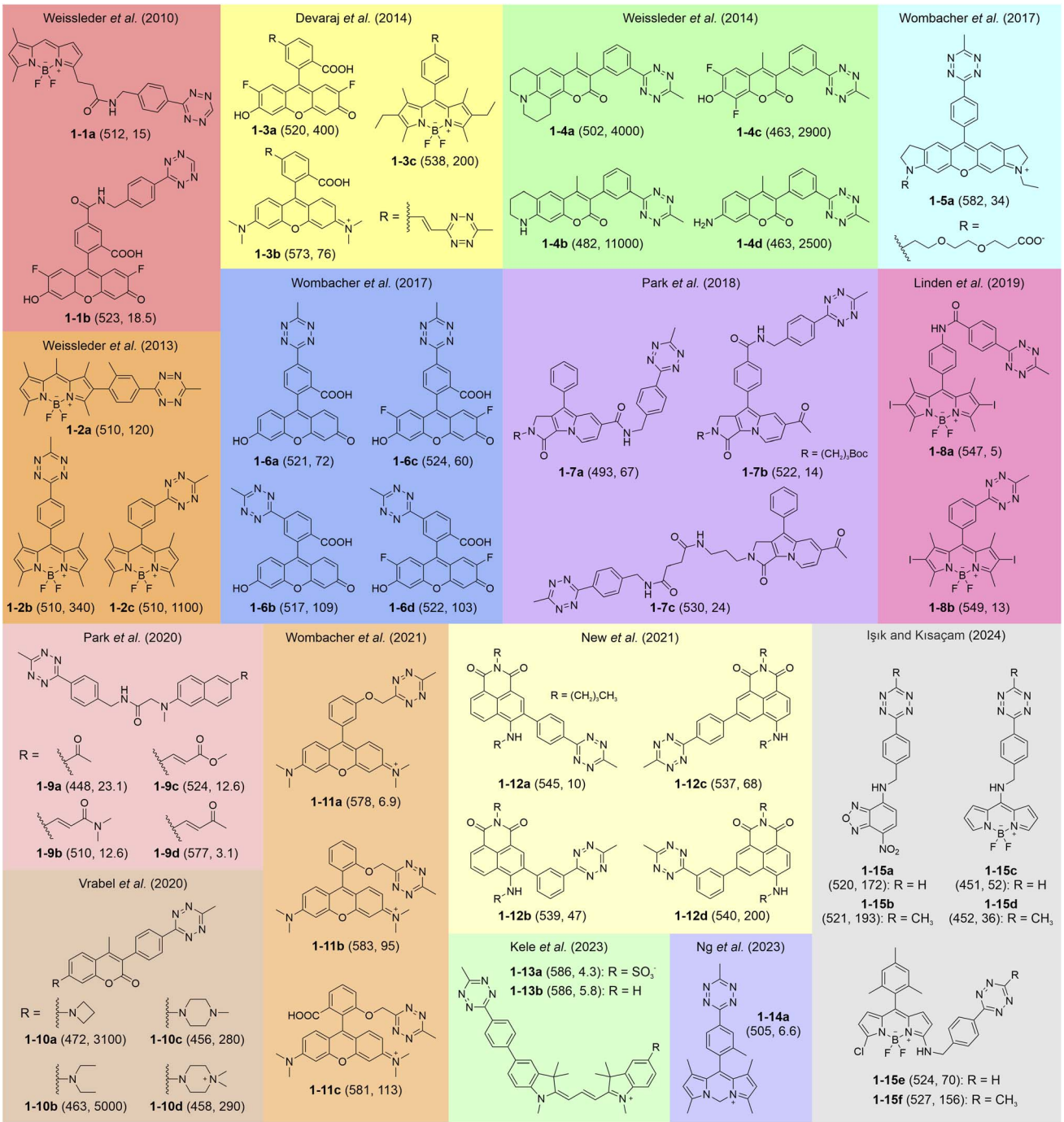

Fig. 1 Representative molecular structures of tetrazine-isolated fluorogenic labels with visible fluorescence. The numbers in each bracket show the λ_{em} (nm) and FE ratios (-fold), respectively. The reaction conditions are listed in Table S1, ESI.†

fluorescence of **1-7b′** by non-radiative decays, resulting in feeble background emissions. In contrast, the subsequent bio-orthogonal reaction with **BCN** realizes the transformation from **1-7b′** into **1-7b′-BCN**, removing tetrazine's dark state and activating the fluorescence of the SF fluorophore (Fig. 2 right). Due to the negligible involvement of tetrazine in SF's conjugation, **1-7b′** and **1-7b′-BCN** share similarities in terms of bright state (de) excitation energies and hole–electron distributions. Therefore, both the peak absorption wavelength (λ_{abs}) and λ_{em} of **1-7b** remain nearly constant regardless of the bio-orthogonal reactions.[66] This ETDS mechanism is applicable across various tetrazine-isolated labels, independent of fluorophore types.

To improve the EnT quenching efficiency and achieve a higher FE ratio after bio-orthogonal reactions, regulating the distance between the main fluorophore and tetrazine is essential. Sauer and co-workers proposed using a flexional spacer to induce a stacking conformation, minimizing the fluorophore-tetrazine distance.[84] Similarly, Wombacher and co-workers

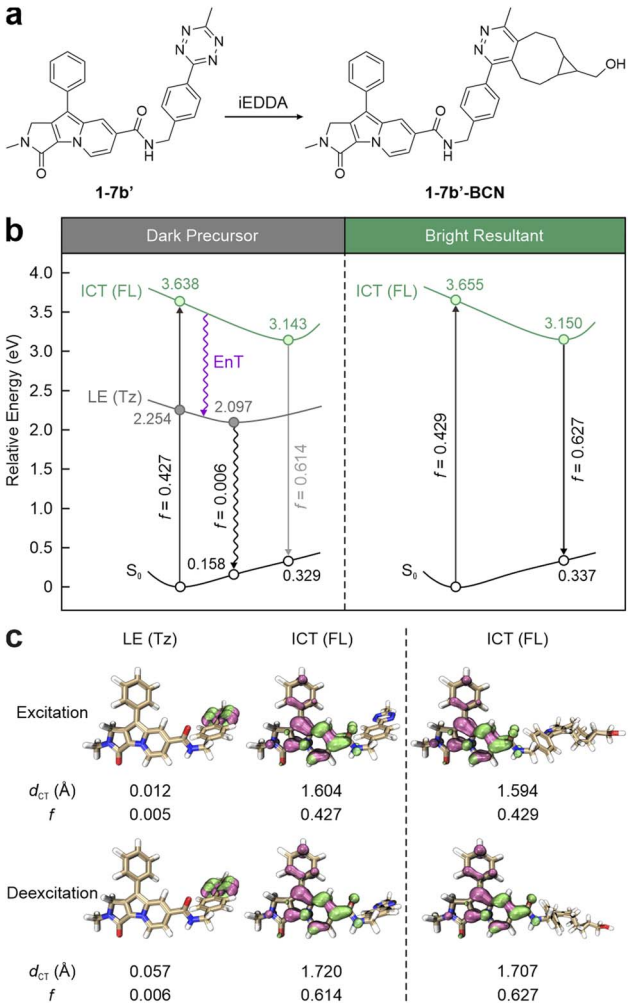

Fig. 2 (a) Molecular structures and (b) photophysical processes with (c) the corresponding hole–electron distributions, charge transfer distances (d_{CT}), and oscillator strength (f) values for different states of **1-7b′** (left) and **1-7b′-BCN** (right) in ethanol (EtOH). Hole – highlighted in mauve; electron – highlighted in green; FL – fluorophore; Tz – tetrazine; S_0 – ground state; LE – locally excited; ICT – intramolecular charge transfer. Reproduced with permission from ref. 53. Copyright 2023, The Royal Society of Chemistry.

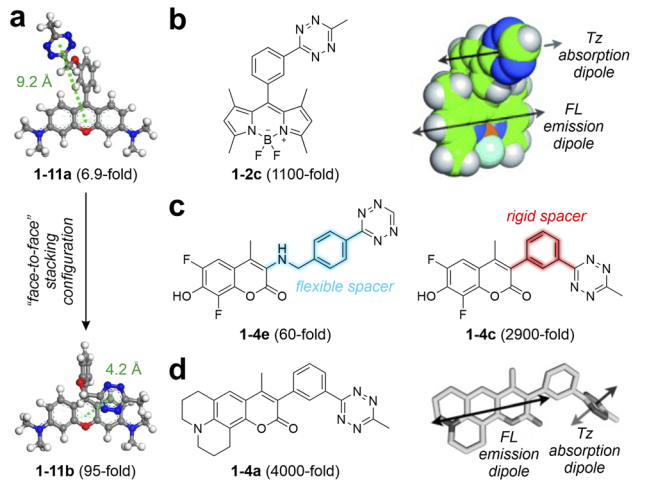

Fig. 3 (a) Optimized ground-state geometries of **1-11a** (left) and **1-11b** (right) with corresponding centroid distances between the main fluorophore and tetrazine in water. (b) Molecular structure (left) and orientation of the FL-Tz transition dipoles (right) of **1-2c**. (c) Molecular structures of **1-4e** (left) and **1-4c** (right). (d) Molecular structure (left) and orientation of the FL-Tz transition dipoles (right) of **1-4a**. FL – fluorophore; Tz – tetrazine. Reproduced with permission from ref. 59, 60 and 73. Copyright 2021, American Chemical Society. Copyright 2013, Wiley-VCH. Copyright 2014, Wiley-VCH.

developed rhodamine-based tetrazine labels with a "face-to-face" stacking arrangement between the main fluorophore and tetrazine.[60] Employing a short and flexible oxymethyl spacer significantly reduced the donor–acceptor distance from 9.2 Å in **1-11a** to 4.2 Å in **1-11b** (Fig. 3a), thereby enabling higher EnT efficiency in **1-11b**. Following bio-orthogonal activations, this design boosted the FE ratio by approximately 13.8-fold.

Moreover, Weissleder and co-workers reported a series of BODIPY-derived tetrazine-isolated labels with robust fluorogenic effects by carefully engineering the spacer group.[59] By connecting the tetrazine moiety to the BODIPY core through a rigid benzene ring, this design minimizes vibrations and long EnT distances typically associated with flexible linkers. This structural choice not only brings the donor and acceptor closer but also optimizes the orientation of their transition dipoles.

The EnT efficiency is enhanced by the parallel alignment of the BODIPY emission and tetrazine absorption dipoles (Fig. 3b). Unlike the modest 15-fold FE ratio displayed by the previous **1-1a**,[58] featuring a long flexible linker, these new labels demonstrated exceptional fluorogenic properties, evidenced by the FE ratio reaching up to 1600-fold post-iEDDA reactions.[59] The excellent fluorogenic signal underscores the potential of spacer engineering in designing tetrazine-isolated BODIPY labels. Inspired by these findings, Weissleder and colleagues extended this approach to different coumarin-based tetrazine labels.[73] Their iEDDA products exhibited a broad emission range from 455 to 502 nm, with ultrahigh FE ratios ranging from 2500 to 11 000-fold. For instance, **1-4c** and **1-4e** share the same core fluorescent skeleton but differ in the spacer (Fig. 3c). The highly rigid spacer in **1-4c** enables a remarkable FE ratio (2500-fold) following bio-orthogonal reactions, in stark contrast to only 60-fold in the post-reacted **1-4e** (using a flexible spacer). This study also emphasized the importance of aligning fluorophore-tetrazine transition dipoles to enhance fluorescence quenching, as illustrated in Fig. 3d. Further expanding this design strategy, New and co-workers[76] applied it to naphthalimide dyes, yielding red-emitting labels with FE ratios up to 200-fold in post-triggered **1-12d**. These studies further underscore the broad applicability of short and rigid spacers, essential for the TBET mechanism, in achieving high fluorogenicity across various tetrazine-isolated systems.

Besides, the FE ratio is also associated with the different bio-orthogonal activation modes for disabling the tetrazine moiety. For example, Weissleder and co-workers demonstrated that after cycloaddition with TCO-OH through the iEDDA reaction, **1-2b** exhibited a 340-fold increment in the FE ratio.[59] In

contrast, Xiao and colleagues reported a distinct 178-fold FE ratio resulting from the photo-fragmentation of the tetrazine moiety in **1-2b**.[41] Similarly, **1-4b** displayed variable FE ratios when subjected to different bio-orthogonal activations.[41,73] These findings highlight the importance of selecting appropriate reaction modes for the bio-orthogonal disintegration of tetrazine to achieve optimal FE ratios.

In designing ETDS-dominated tetrazine labels, reducing the fluorophore-tetrazine distance is essential for efficient EnT, thereby effectively minimizing background noise and enabling substantial FE ratios upon bio-orthogonal reactions. This regulation of donor–acceptor distances stimulated the emergence of next-generation tetrazine labels, specifically tetrazine-integrated designs with "zero" donor–acceptor distance. These innovative labels introduce a distinct quenching pathway that diverges from traditional ETDS mechanisms, representing a significant advancement in fluorogenic labelling technology.

3.2 Internal conversion to a dark state (ICDS) in tetrazine-integrated labels

The labels discussed in Section 3.1 require spacers of varying sizes to attach the tetrazine to different fluorophores, effectively isolating the π-conjugations of the two fragments. While a short EnT distance facilitates fluorescence quenching before and enhancement after bio-orthogonal reactions, a novel approach has emerged to further minimize the distance in traditional tetrazine labels. This method directly incorporates tetrazine into the skeleton of the main fluorophore, creating a fused π-conjugated system with "zero" donor–acceptor distance (Fig. 4).

Vrabel *et al.* proposed a design approach to develop tetrazine-merged fluorogenic labels by regulating the substituent groups on both sides of the tetrazine (**2-1a–i**).[61] This method effectively integrated the tetrazine fragments into the conjugated systems of the generated labels.[62–65] These multi-coloured labels exhibited strong potential for bio-orthogonal imaging applications. Other groups have reported similar tetrazine-

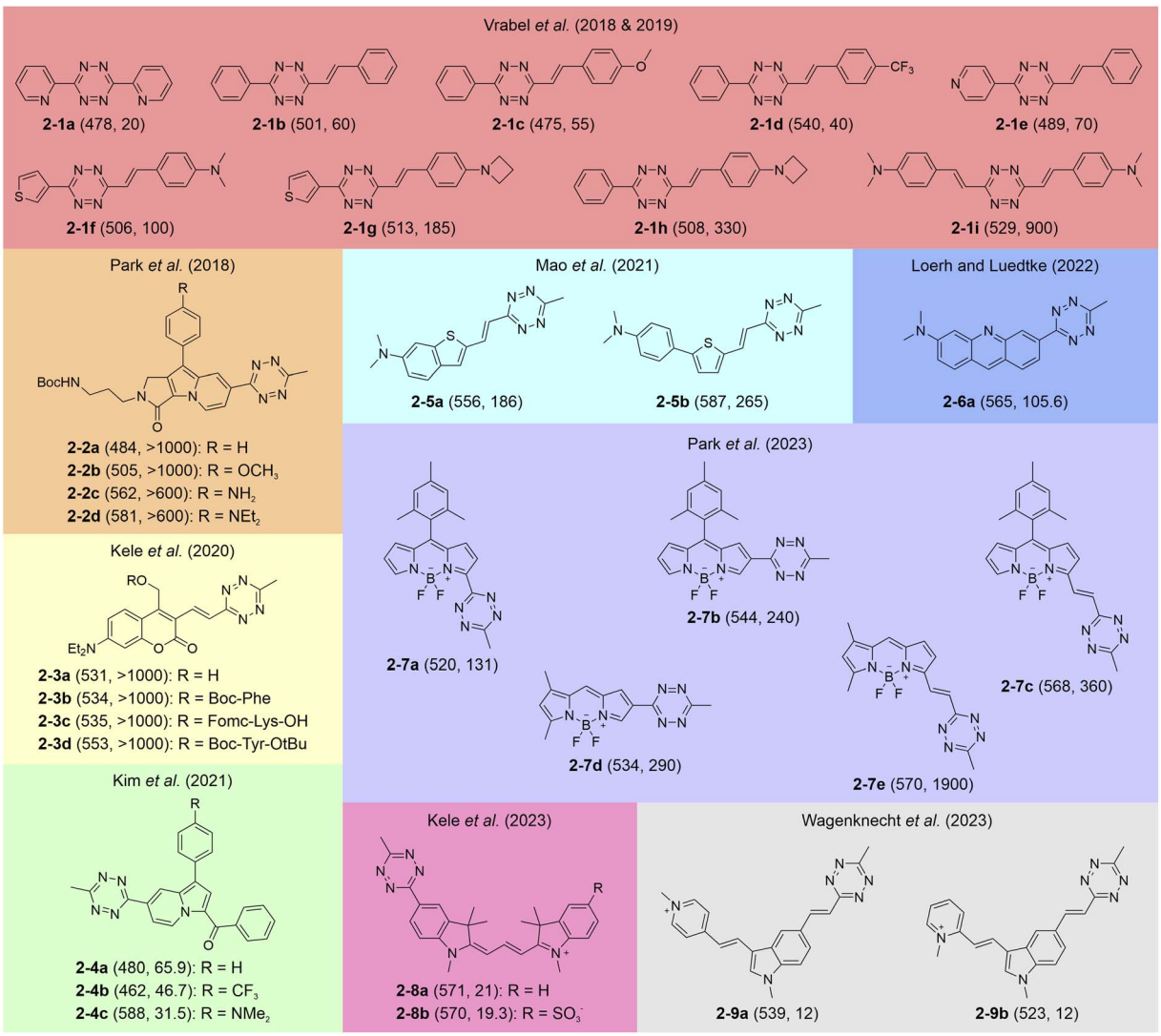

Fig. 4 Representative molecular structures of tetrazine-integrated fluorogenic labels with visible fluorescence. The numbers in each bracket show the λ_{em} (nm) and FE ratios (-fold), respectively. The reaction conditions are listed in Table S2, ESI.†

fused fluorophores. For instance, Park *et al.* introduced the monochromophoric design rule by directly attaching tetrazine fragments to various SF fluorophores (**2-2a–d**),[66] yielding labels with emission ranges from 484 to 581 nm and FE ratios exceeding 600-fold. This fusion strategy also finds its generalizability in various dye families (Fig. 4 and S2, ESI†), covering coumarin (**2-3a–d**),[85] kaleidolizine (KIz; **2-4a–c**),[86] Huaxi-Fluor (HX; **2-5a,b**),[87] acridine (**2-6a**),[88] BODIPY (**2-7a–e**),[89] cyanine (**2-8a,b**),[77] cyanine-styryl (**2-9a,b**),[90,91] and 2-(4-(dimethylamino) styryl)-4*H*-chromen-4-one (DMAC; **2-10a,b**).[42]

Liu and co-workers identified a generalizable mechanism behind the fluorogenicity of tetrazine-integrated labels, termed internal conversion to a dark state (ICDS).[53] The simplified **2-2a** (**2-2a′**) was selected as a representative example (Fig. 5a). This example demonstrates how the direct attachment of tetrazine to the SF fluorophore enables significant electronic interactions between the two moieties. Unlike **1-7b′**, where the tetrazine is geometrically and electronically isolated from the SF fluorophore, **2-2a′** exhibits a planar conformation, allowing efficient electronic communication across the entire label. The photophysical analysis revealed that the most stable state is still the tetrazine-induced dark LE state ($f = 0.005$; $d_{CT} = 0.051$ Å) during the photoexcitation, similar to that of **1-7b′** (Fig. 5 left). Situated 1.020 eV above this dark state is a bright state ($f = 0.377$; Fig. 5b left), which dominates the light absorbance. Yet, in contrast to the tetrazine-isolated configuration, where the ICT state is merely induced by the SF fragment in **1-7b′**, the π–π* transition of **2-2a′** extends across the entire label. This indicates a significant contribution of tetrazine to the bright state transition. The integrated nature of tetrazine and SF in **2-2′** is also reflected by a 0.349 eV reduction in the S_2 vertical excitation energy compared to that of **1-7b′**, where only the SF moiety participates in the bright state transition. This alteration is also corroborated by the experimental data, *i.e.*, the λ_{abs} of **2-2a** (415 nm) is longer than that of **1-7b** (375 nm) by 40 nm.[66] Hence, the integrated π-conjugation renders **2-2a′** as a single-entity system. Following geometric relaxation, the bright state energy is positioned 0.754 eV above the dark one. The energy absorbed by the entire label (involving the SF fragment and tetrazine) transitions to its tetrazine fragment *via* internal conversion (IC), resulting in the fluorescence quenching of **2-2a′**.

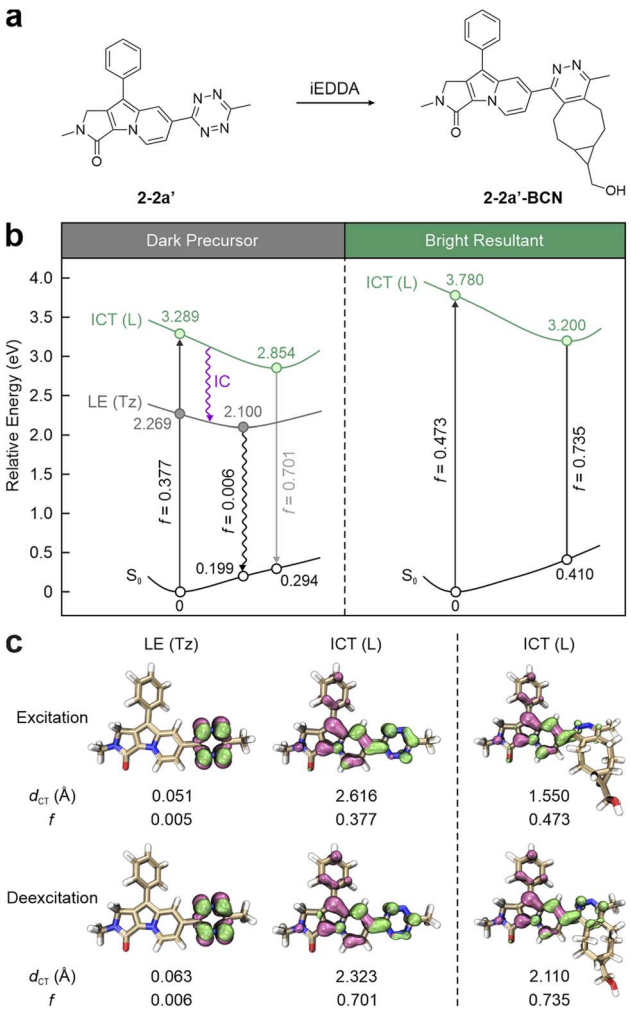

Fig. 5 (a) Molecular structures and (b) photophysical processes with (c) corresponding hole–electron distributions, d_{CT}, and f values for different states of **2-2a′** (left) and **2-2a′-BCN** (right) in EtOH. Hole – highlighted in mauve; electron – highlighted in green; L – entire label; Tz – tetrazine; S_0 – ground state; LE – locally excited; ICT – intramolecular charge transfer; ET – electron transfer; PET – photoinduced electron transfer; CI – conical intersection. Reproduced with permission from ref. 53. Copyright 2023, The Royal Society of Chemistry.

In contrast, the BCN-triggered bio-orthogonal reaction disrupts the dark state associated with tetrazine, unleashing the fluorescence through a new bright π–π* transition state ($f = 0.735$; Fig. 5b right). It is worth noting that the tetrazine residue in **2-2a′-BCN** also has clear contributions to this bright state transition (Fig. 5c right). The bio-orthogonal reactions modify the structure of tetrazine, thus increasing the bright state energy from 3.289 eV in the precursor to 3.780 eV in the post-reacted label. This elevation is corroborated by the hypsochromically shifted λ_{abs} from 415 nm in **2-2a** to 386 nm in its iEDDA product.[66] This spectral variation distinguishes these ICDS labels from ETDS-type tetrazine labels. In ICDS labels, tetrazine residues contribute to bright state transitions, considerably impacting the absorption spectrum post-reaction.

Inspired by the ICDS mechanism and the integrated conjugation characteristic, Liu's group proposed several fluorophore design strategies. In one approach, they introduced an additional coumarin molecule at the right end of **2-3a**, positioning the tetrazine centrally within the entire label to extend the π-conjugation network (**2-11a**; Fig. 6a).[53] Following the BCN adduction, this approach leads to bathochromic shifts in both λ_{abs} and λ_{em} compared to those of **2-3a-BCN**, as seen in **2-11a-BCN** (Fig. 6b and S3, ESI†). Meanwhile, they modified the π-bridge structure of **2-5b** by swapping the positions of the $-CH_2-$ unit with the thiophene ring, yielding its constitutional isomer (**2-11b**; Fig. 6c).[53] This alteration promotes quinoidization within the π-bridge, greatly enhancing ICT and reducing the bright state energy.[92] As a result, both λ_{abs} and λ_{em} of **2-11b-BCN** are significantly redshifted compared to those of **2-5b-BCN** (Fig. 6d and S3, ESI†).

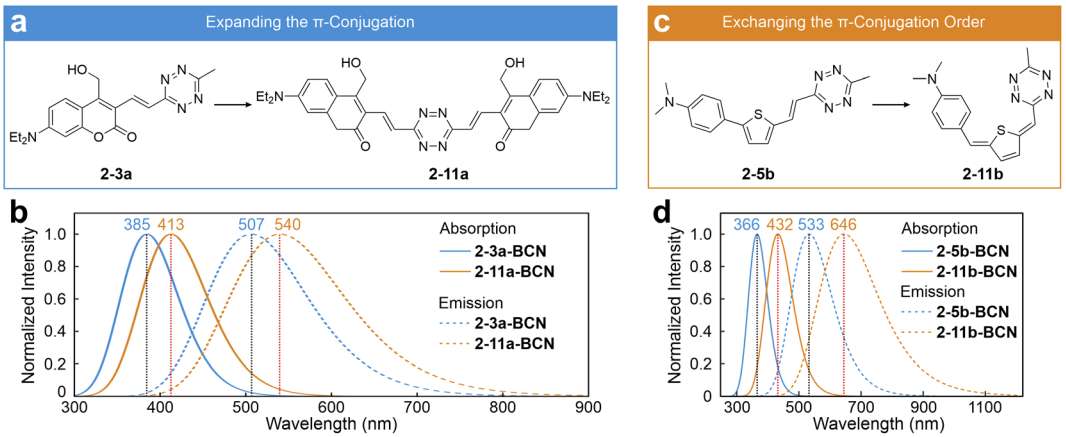

Fig. 6 Design strategies of (a) expanding the π-conjugation and (c) exchanging the π-conjugation order to induce redshifted tetrazine dyes. Calculated absorption and emission spectra of (b) **2-3a-BCN**/**2-11a-BCN** and (d) **2-5b-BCN**/**2-11b-BCN** in EtOH. Reproduced with permission from ref. 53. Copyright 2023, The Royal Society of Chemistry.

Although the tetrazine-based fluorogenic labels generally exhibit favorable FE ratios in the visible spectrum, these ratios significantly decrease when their emission wavelengths shift to deep-red and NIR regions.[93,94] This reduction is due to the inhibition of the energy flows, either *via* EnT or IC.[54] As discussed in Section 3, both ETDS and ICDS mechanisms rely on a stable dark state, generated by the tetrazine's n–π* transition, as an energy "sink", with the bright π–π* state of the fluorophore acting as the energy "source". This energy positioning allows effective fluorescence quenching through sufficient EnT/IC from the main fluorophore (or the entire label) to the tetrazine, resulting in minimal background emissions (Scheme 3 left). Nevertheless, the excitation/deexcitation energy of the bright state drops on bathochromically shifting the $\lambda_{abs}/\lambda_{em}$ of the main fluorophore (or the entire label). Yet, the tetrazine-induced dark LE state remains almost constant. When the bright state approaches the dark one, state crossing during geometric relaxation may invert their positions (Scheme 3 middle). This swap reduces energy flow efficacy and suppresses the fluorescence quenching effect. Furthermore, in a typical NIR dye, the bright state is usually more stable than tetrazine's dark state (Scheme 3 right), making EnT and IC energetically unfavorable and decreasing the fluorescence quenching efficiency. This analysis highlights the intrinsic challenges in developing tetrazine-functionalized labels with high fluorogenicity in the deep-red and NIR regions.

Nonetheless, several tetrazine-isolated and tetrazine-integrated fluorogenic labels with deep-red to NIR emissions have been developed in recent years, effectively circumventing the energy requirements described above. These intriguing advancements have motivated researchers to expand upon existing mechanisms, further enhancing our understanding of fluorescence quenching processes in long-wavelength tetrazine labels and improving their fluorogenic properties.

4. Charge separation dominates fluorogenicity in deep-red and near-infrared (NIR) tetrazine labels

4.1 Photoinduced electron transfer (PET) in tetrazine-isolated labels

Several studies have reported tetrazine-isolated labels featuring deep-red to NIR emissions following iEDDA reactions (Fig. 7). In

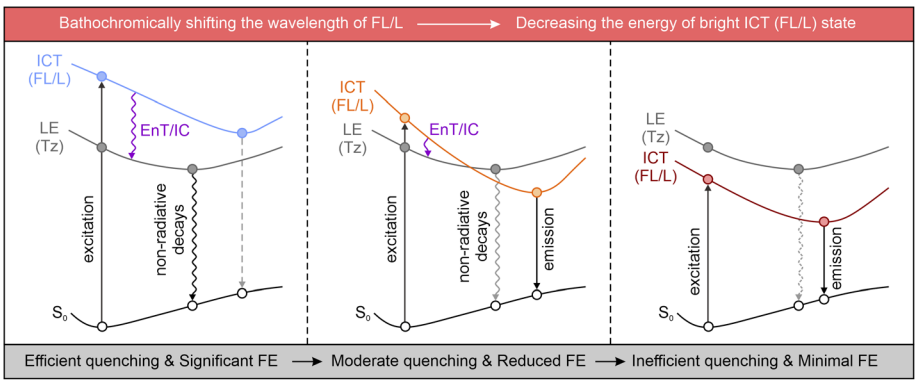

Scheme 3 Wavelength/energy level-dependent photophysical processes in tetrazine-based labels. FL – fluorophore; Tz – tetrazine; L – entire label; S_0 – ground state; ICT – intramolecular charge transfer; LE – locally excited; EnT – energy transfer; IC – internal conversion.

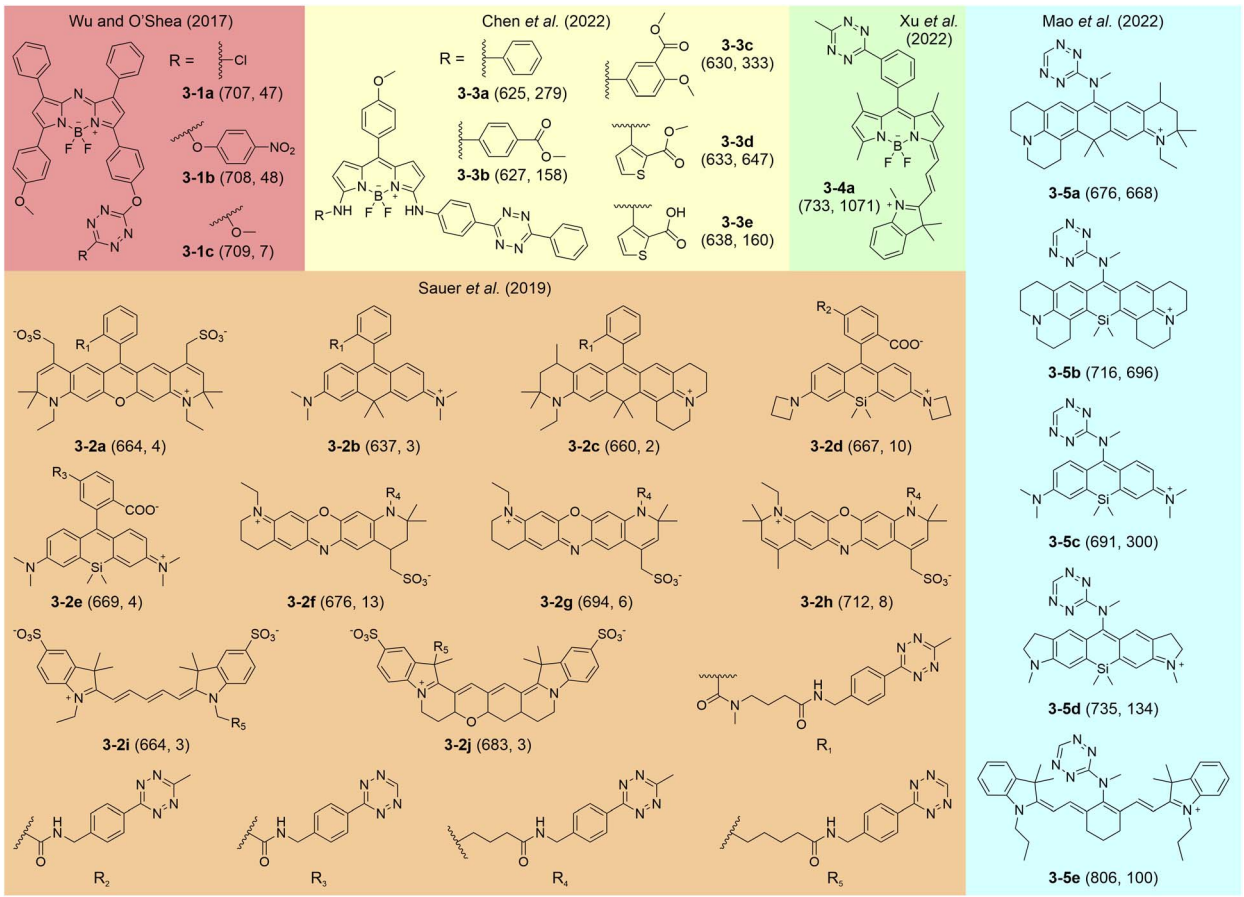

Fig. 7 Molecular structures of representative tetrazine-isolated labels with deep-red-NIR emissions. The numbers in each bracket show the λ_{em} (nm) and FE ratios (-fold), respectively. The reaction conditions are listed in Table S3, ESI.†

2017, Wu and O'Shea pioneeringly proposed the generation of NIR-fluorescent tetrazine-isolated labels by linking tetrazine to different aza-BODIPY skeletons (**3-1a–c**).[95] These labels displayed moderate FE ratios from 7 to 48-fold with average λ_{em} values of around 708 nm. They suggested that photoinduced electron transfer (PET) might contribute to the fluorescence quenching in these precursors. Sauer *et al.* subsequently reported rhodamine, phenoxazine, and cyanine-based tetrazine-isolated dyes (**3-2a–j**), showcasing a broad emission range from 637 to 712 nm and discernible FE ratios (2–13-fold).[84] Chen and co-workers successfully developed BODIPY-derived tetrazine labels emitting across deep-red to NIR regions and achieving impressive FE ratios between 158 and 647-fold (**3-3a–e**).[96] Xu and colleagues later designed a BODIPY-cyanine tetrazine label (**3-4a**), displaying a redshifted λ_{em} at 733 nm and a remarkable FE ratio (1073-fold).[97] Mao *et al.* carried forward this approach to rhodamine and cyanine families, producing compounds with far-red to NIR emissions up to 806 nm and FE ratios as high as 1459-fold (**3-5a–e**).[94] Yet, the quenching mechanism of these tetrazine-isolated labels in deep-red and NIR spectra remains controversial. The unclear correlation between their fluorogenicity and molecular structures hampers further amelioration.

In 2024, Shen and co-workers conducted comprehensive computational investigations on these labels, rationalizing that PET is the dominant mechanism responsible for fluorescence quenching in tetrazine-isolated labels emitting deep-red-to-NIR fluorescence.[54] Their findings suggest that even when the ETDS is suppressed, the fluorescence of these precursors can still be quenched by PET. Upon removal of the tetrazine fragments, this quenching channel is blocked, enabling fluorescence recovery in the post-reacted labels.

For instance, in label **3-4a** reported by Xu and co-workers (Fig. 8a),[97] the tetrazine is installed on the main fluorophore, *i.e.*, a NIR BODIPY-cyanine fragment, *via* a benzene spacer, forming a dual-entity system (with two separate π-conjugation networks: one for the fluorophore and the other for the tetrazine). During photoexcitation and deexcitation, the tetrazine-induced dark state lies at higher energies than the fluorophore-caused bright state (Fig. 8b left). To be specific, the tetrazine leads to an elevated dark LE state, described by a negligible f value (0.007) and a small d_{CT} (0.038 Å) upon vertical excitation (Fig. 8c left). Conversely, the π–π* transition of the BODIPY-cyanine skeleton generates a bright ICT state (f = 1.148), contributing to light absorption. This bright state is beneath the dark one by 0.258 eV and stabilizes at 2.279 eV following geometric relaxation, prohibiting EnT to the tetrazine. However, another dark state (f = 0) is discovered 0.245 eV below the bright ICT state. In its transition, the hole is delocalized throughout the main fluorophore. In contrast, the electron concentrates on

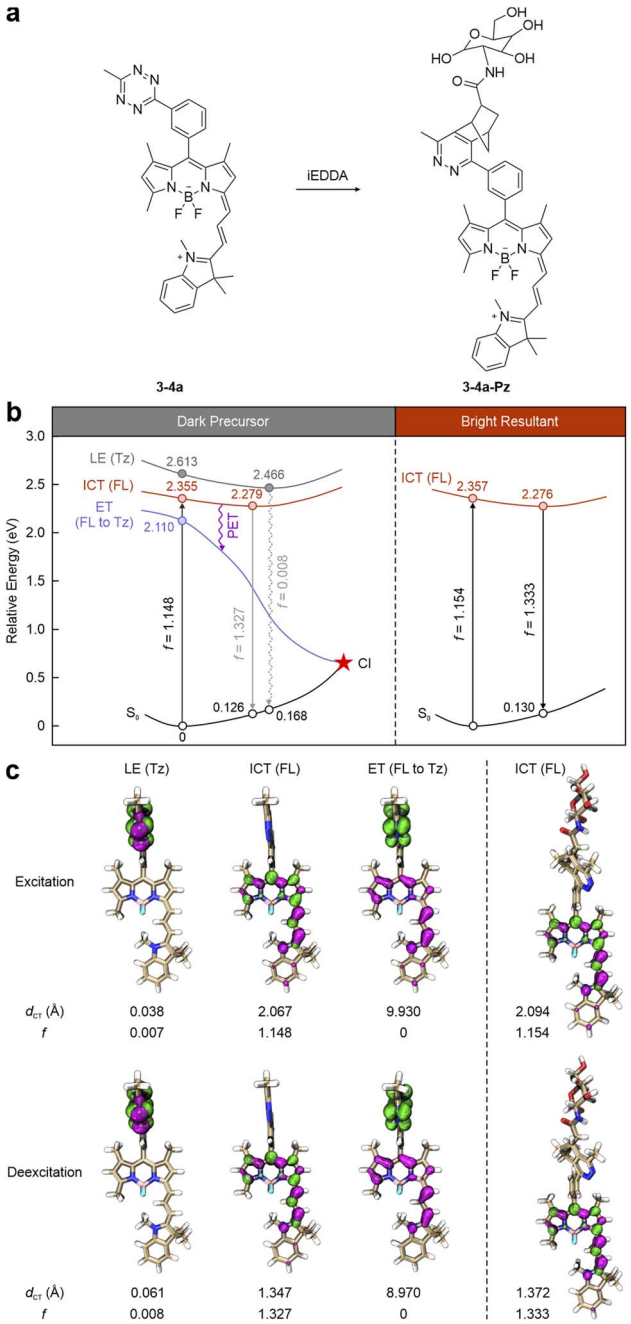

Fig. 8 (a) Molecular structures and (b) photophysical processes with (c) corresponding hole–electron distributions, d_{CT}, and f values for different states of **3-4a** (left) and **3-4a-Pz** (right) in dimethyl sulfoxide (DMSO). Hole – highlighted in pink; electron – highlighted in green; FL – fluorophore; Tz – tetrazine; S_0 – ground state; LE – locally excited; ICT – intramolecular charge transfer; ET – electron transfer; PET – photoinduced electron transfer; CI – conical intersection. Reproduced with permission from ref. 54. Copyright 2024, The Royal Society of Chemistry.

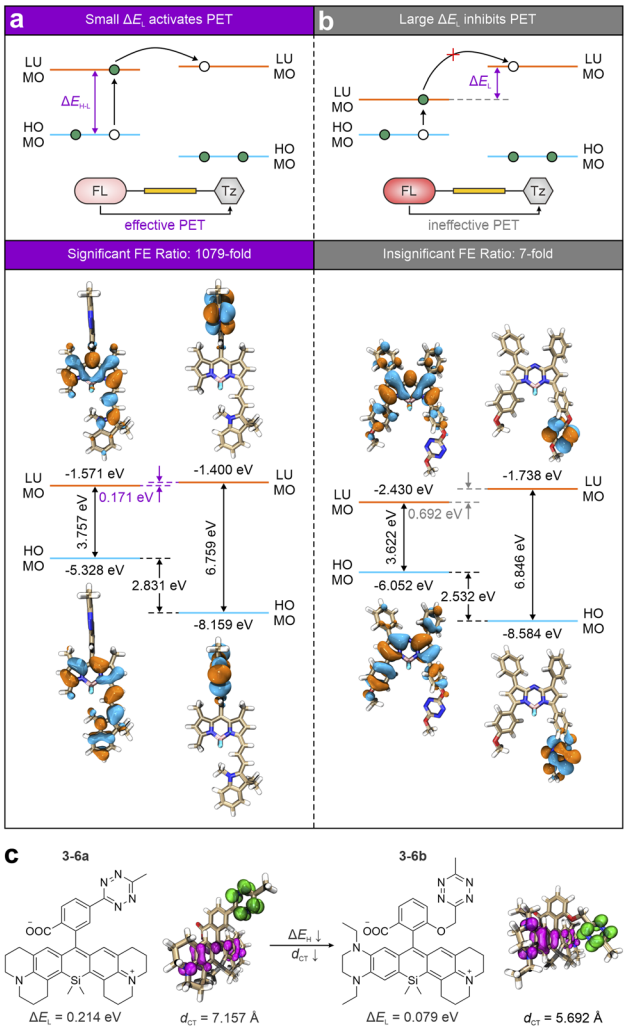

Fig. 9 Schematic illustrations of (a) effective and (b) ineffective PET activations based on the frontier molecular orbitals (top) with corresponding representatives (bottom) of deep-red-to-NIR tetrazine-isolated labels. (c) Molecular structures and hole–electron distributions (top) with corresponding ΔE_L and d_{CT} (bottom) of the ET states for **3-6a** and **3-6b** during the photoexcitation processes in DMSO. Hole – highlighted in pink; electron – highlighted in green. Reproduced with permission from ref. 54. Copyright 2024, The Royal Society of Chemistry.

the tetrazine fragment, illustrating a complete charge transfer feature with a large d_{CT} (9.930 Å), indicative of the electron transfer (ET) phenomenon. Hence, BODIPY-cyanine and tetrazine can be viewed as the electron-donor and electron-acceptor, respectively. The PET pathway is activated to quench the fluorescence of the main fluorophore, resulting in **3-4a** emitting almost no fluorescence. The subsequent iEDDA reaction with tetrazine eliminates the dark state (Fig. 8 right). Moreover, both excitation and deexcitation/emission energies remain almost the same after the iEDDA reaction, as the tetrazine moiety and residue do not participate in the conjugated system of the BODIPY-cyanine dye.

It is worth noting that PET has been identified as the leading quenching mechanism in the deep-red-to-NIR tetrazine-isolated labels. However, its efficiency remains restricted in some scenarios. This efficiency, often reflected by the FE ratios upon bio-orthogonal activations, is strongly influenced by the electronic energy difference (ΔE_L) between the lowest unoccupied molecular orbitals (LUMOs) of the main fluorophore (acting as an electron-donating group) and tetrazine (serving as an

electron-withdrawing group; Fig. 9a top).[54] A large ΔE_L suggests that the LUMO energy of tetrazine is much higher than that of the main fluorophore, thereby inhibiting the ET and reducing the quenching effect (Fig. 9b top). For example, due to variations in ΔE_L, **3-4a** and **3-1c** bio-orthogonal resultants displayed starkly different FE ratios, *i.e.*, 1079-fold and 7-fold, respectively. With a small ΔE_L of 0.171 eV, **3-4a** shows more effective PET quenching (Fig. 9a bottom). In comparison, the ΔE_L value of **3-1c** reaching 0.692 eV (Fig. 9b bottom) results in a less efficient PET, leading to higher background emissions and a lower FE ratio. Besides, shortening the ET distance is also crucial for promoting sufficient PET quenching.

These two factors, *i.e.*, minimal ΔE_L and reduced ET distance, are essential for systematically optimizing the PET efficiency in NIR tetrazine-isolated labels. To achieve this, Shen *et al.* demonstrated a design strategy by structurally modifying silicon–rhodamine (Si–rhodamine; Fig. 9c).[54] By introducing dual electron-donating groups to the main skeleton of **3-6a**, the gap between the highest occupied molecular orbital (HOMO) and LUMO (ΔEH-L) is reduced to the redshifted λ_{abs} and λ_{em} in the generated **3-6b**. Meanwhile, this modification also lowers ΔE_L to 0.079 eV. Additionally, the close stacking configuration between the modified Si–rhodamine and tetrazine reduces the ET distance from 7.157 Å to 5.692 Å. Therefore, this approach,

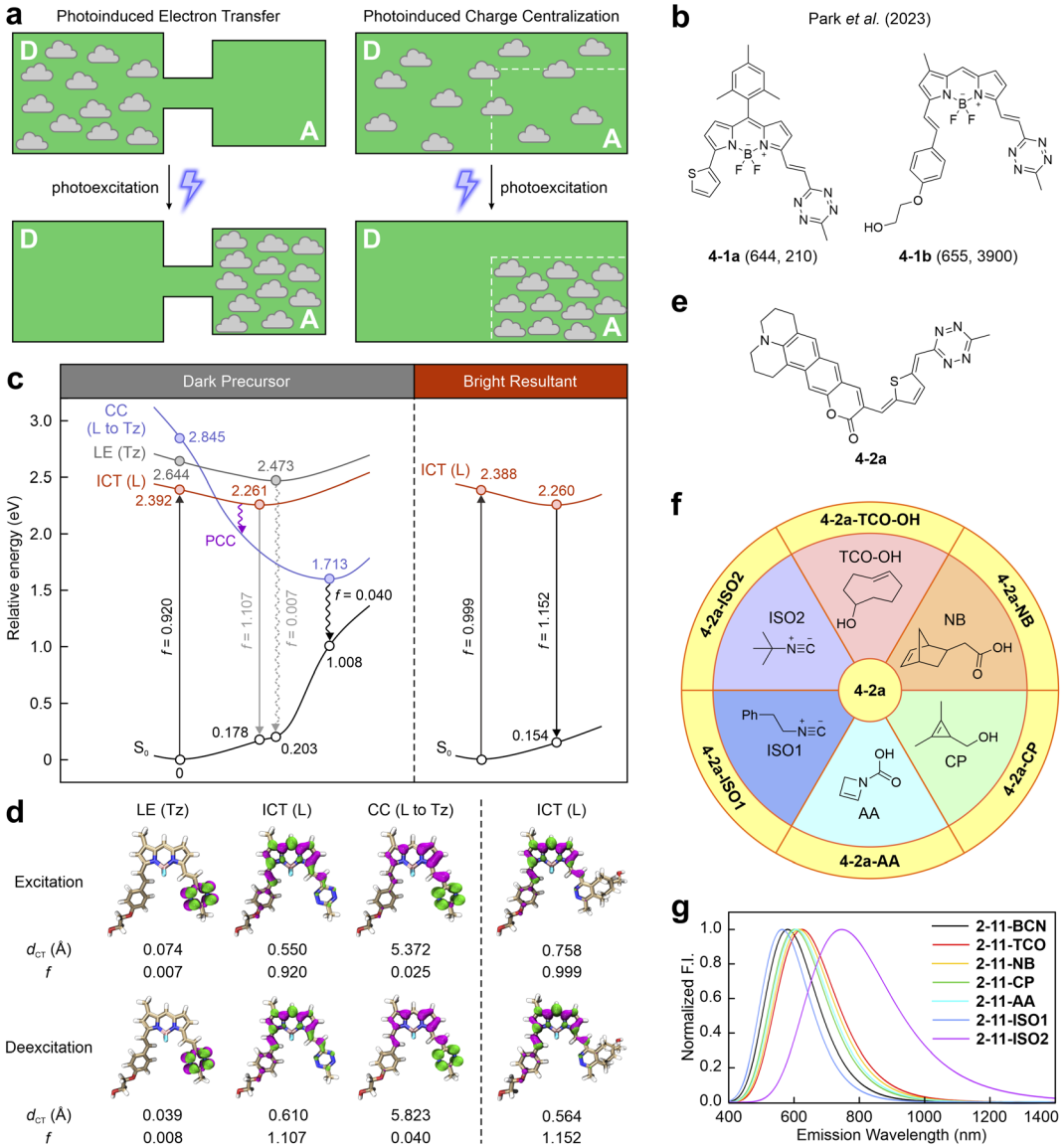

Fig. 10 (a) Comparison between PET and PCC. (b) Molecular structures of **4-1a** and **4-1b**. The numbers in each bracket show the λ_{em} (nm) and FE ratios (-fold), respectively. The reaction conditions are listed in Table S3, ESI.† (c) Photophysical processes with (d) corresponding hole–electron distributions, d_{CT}, and *f* values for different states of **4-1a** before (left) and after (right) the iEDDA reaction in water. Hole – highlighted in pink; electron – highlighted in green; L – entire label; Tz – tetrazine; S_0 – ground state; LE – locally excited; ICT – intramolecular charge transfer; ET – electron transfer; PET – photoinduced electron transfer; CI – conical intersection. (e) Molecular structure of **4-2a**; (f) demonstration of bio-orthogonal reactions between **4-2a** with various counterparts; (g) calculated normalized emission spectra of seven post-reacted **4-2a** in water. Reprinted with permission from ref. 55. Copyright 2024, American Chemical Society.

addressing both the energy level alignment and electron transfer distance, shows promise for enhancing the wavelength and FE ratios of tetrazine-isolated labels. Similarly, Mao and co-workers engineered a mono-substituted amino-tetrazine at the *meso*-position of various rhodamine and cyanine scaffolds to further minimize the ET distance (Fig. 7).[94] The resulting molecules (**3-5a–e**) exhibit substantial turn-on ratios, demonstrating the efficacy of this design strategy.

4.2 Photoinduced charge centralization (PCC) in tetrazine-integrated labels

Recently, Shen *et al.* unveiled a distinctive charge separation pathway called photoinduced charge centralization (PCC; Fig. 10a).[54] This pathway was serendipitously discovered while investigating the photophysical properties of tetrazine-integrated fluorogenic labels in the visible region. Further studies confirmed that the PCC mechanism predominantly quenches deep-red-to-NIR fluorescence in tetrazine-integrated labels with fused π-conjugations (Fig. 10b).[55]

For example, in the NIR tetrazine-merged label **4-1b**, reported by the group of Park,[89] tetrazine is directly bonded to the main fluorophore, forming a fused π-conjugated system. During vertical excitation, the most stable state is the bright ICT state generated by the π–π* transition spanning the entire label (Fig. 10c and d left). The tetrazine-induced dark LE state sits above the bright state by 0.252 eV during excitation and 0.212 eV during deexcitation, thereby suppressing IC from the entire label to the tetrazine. Yet, after geometric relaxation, a low-energy dark charge centralization (CC) state turns out to be the most stable one at 1.713 eV. In this CC state, the hole is delocalized throughout the entire label, while the electron concentrates on the tetrazine, demonstrating tetrazine's significant role in the charge distribution of both the hole and the electron. Consequently, photoexcitation drives charge transfer from the entire label to concentrate on its internal tetrazine. The dark CC state effectively quenches the fluorescence of the entire label. Like other tetrazine labels, upon activation by BCN, the resulting compound exhibits strong fluorescence due to the inhibition of PCC (Fig. 10c and d right and Fig. S4, ESI†).

Although the PCC process is similar to the well-known PET, it possesses several distinguishing features. PET necessitates the isolation of tetrazine from the main fluorophore, ensuring that their π-conjugations remain independent (Fig. 10a left). Upon photoexcitation, almost complete charge separation occurs from the main fluorophore to the tetrazine, with almost no spatial overlap in the hole–electron distribution of the ET state. In contrast, PCC involves a unified π-conjugation system, where tetrazine is fused with the fluorophore both geometrically and electronically (Fig. 10a right). Upon photoexcitation, charge transfer occurs from the entire label to tetrazine, forming a CC state with considerable overlap between hole and electron distributions. This overlap region typically resides in the tetrazine fragment.

This unique PCC pathway not only enhances the mechanistic understanding of fluorogenicity in long-wavelength tetrazine-fused labels but also enriches photophysics and physical chemistry by introducing a novel photoinduced charge separation process. However, reports on PCC-driven tetrazine-integrated dyes are scarce. The applicability and generalizability of this mechanism in regulating the fluorogenicity of long-emission tetrazine labels remains an area that warrants further experimental investigations.

To this end, building on the PCC mechanism and the conjugation-fused structure, Shen and Liu theoretically

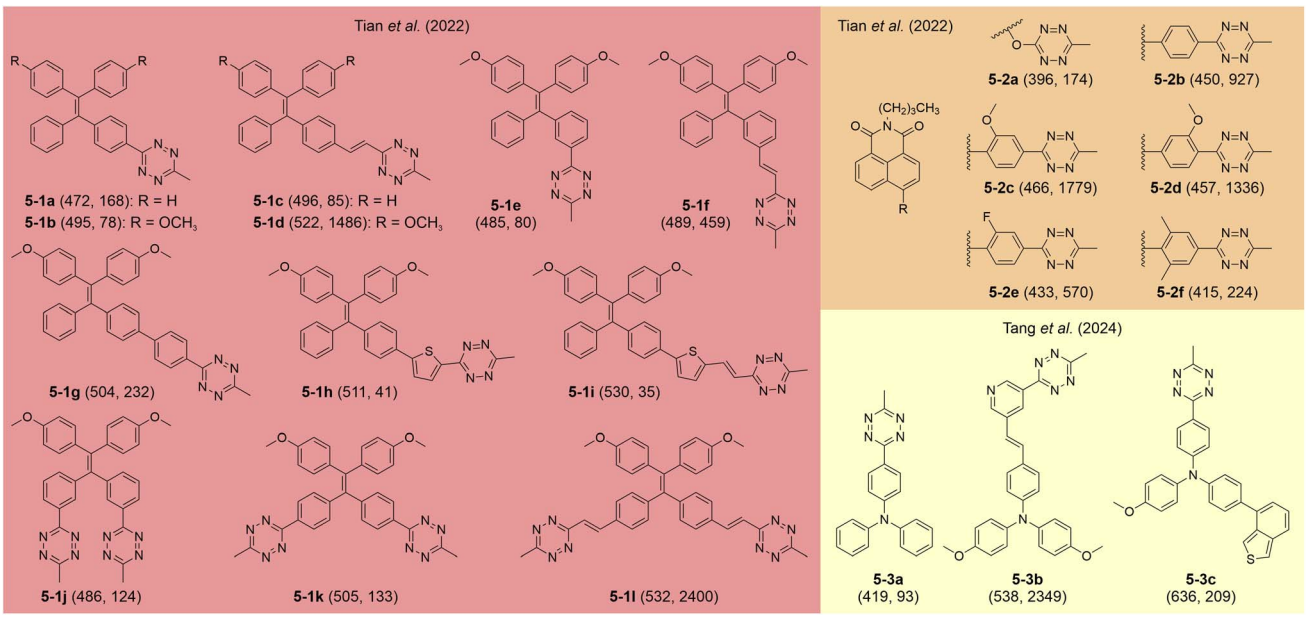

Fig. 11 Molecular structures of representative tetrazine labels with aggregation features. The numbers in each bracket show the λ_{em} (nm) and FE ratios (-fold), respectively (at the aggregate phases). The reaction conditions are listed in Table S4, ESI.†

designed a tetrazine-integrated label featuring a quinoidal π-conjugation bridge to achieve redshifted wavelengths (Fig. 10e).[55] Their simulations modelled interactions between the label and various counterparts (Fig. 10f), and produced seven distinct compounds with varied absorption and emission wavelengths (Fig. 10g and S5, ESI†). These differences stem from the diverse π–π* bright state transitions, affected by the electron-withdrawing strengths of the tetrazine residues. Interestingly, post-reaction labels emit multicolor fluorescence based on their specific triggers, potentially enabling multiplex NIR bio-orthogonal imaging and the simultaneous visualization of various intracellular processes. This approach highlights the versatility of the PCC mechanism and its potential to advance intracellular NIR-imaging technologies.

5. Influence of aggregation/disaggregation on the fluorescence modulation of tetrazine labels

5.1 "Matthew effect": aggregation-enhanced fluorogenicity in tetrazine labels

In recent years, researchers have explored the attachment of tetrazine to various aggregation-induced emission luminogens (AIEgens), including **2-4a–c** as shown in Fig. 4, as well as **5-1a–i**, **5-2a–f**, and **5-3a–c** in Fig. 11. Kim and co-workers proposed that tetrazine-modified AIE labels could serve as effective fluorogenic agents for film-state and *in vivo* imaging applications.[86] These labels were synthesized by conjugating tetrazine at different positions on KIz skeletons (Fig. 4), leading to distinctive behaviors that deviate from conventional click activation responses. For instance, **2-4a** does not display a strong FE ratio in tetrahydrofuran (THF) after the iEDDA reaction (Fig. 12a). However, adding water promotes aggregation, producing a blueshifted λ_{em} and a 22.5-fold FE increment (Fig. 12a and b). In solid-state applications, tetrazine-AIE labels exhibited substantial FE responses (up to 67.8-fold) following reactions with *trans*-cyclooctene (TCO) in spin-coated films, further validating their aggregation-induced emission properties. Coincidentally, Tian *et al.* advanced this area by developing a set of tetrazine-linked tetraphenylethylene (TPE) fluorophores as AIE bio-orthogonal fluorogenic labels (**5-1a–j**; Fig. 11).[98] Upon activation, these labels exhibited tunable emissions ranging from 472 to 597 nm and remarkable FE ratios of up to 2400-fold in aggregate phases. For instance, after undergoing BCN adduction in DMSO, **5-1d** displayed minimal fluorescence. However, increasing the water fraction caused a dramatic FE increase, reaching a 1486-fold enhancement (Fig. 12c and d). Meanwhile, they further innovated by designing a "double-quenched" system in which two tetrazine groups were attached to distinct phenyl rings on a TPE fragment (**5-1j–i**; Fig. 11). In this setup, the destruction of one tetrazine group did not yield significant FE. A strong FE response can be observed only by disrupting both tetrazine groups, demonstrating a sequential activation strategy. Moreover, these BCN adducts showed marked AIE effects, with FE ratios increasing alongside water content. Building on this foundation, Tian and collaborators developed

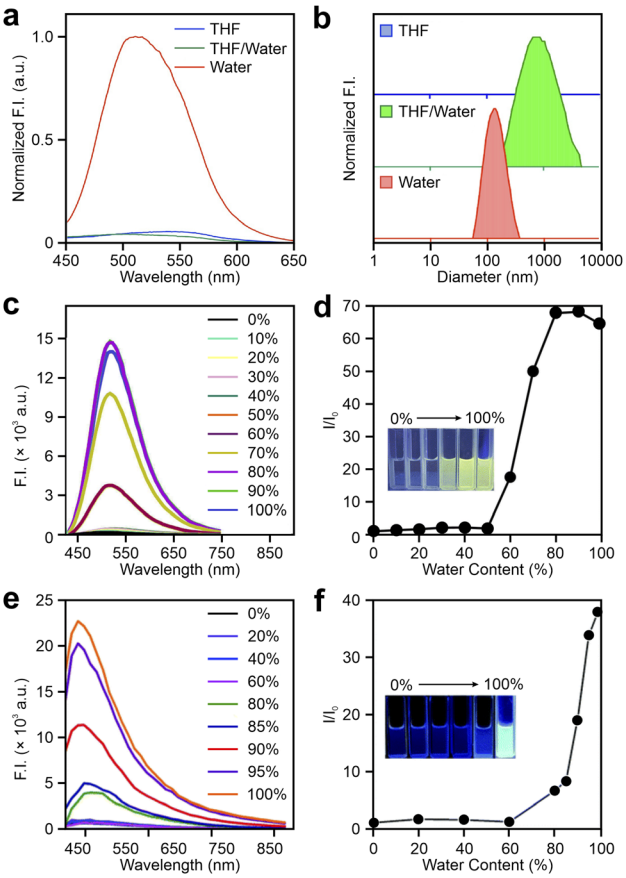

Fig. 12 (a) Emission spectra and (b) dynamic light scattering results of **2-4a** after reacting with TCO in THF, a THF/water mixture (v/v = 1/1), and water. Emission spectra of (c) **5-1d** and (e) **5-2a** after reacting with BCN in DMSO–water mixtures with various water contents; the water content-dependence of relative fluorescence intensities of BCN-triggered (d) **5-1d** and (f) **5-2a**; the inset image shows the physical appearances of BCN-triggered labels in different DMSO–water mixtures under UV light. Reproduced with permission from ref. 86, 98 and 99. Copyright 2021, Elsevier. Copyright 2022, The Royal Society of Chemistry. Copyright 2022, The Royal Society of Chemistry.

naphthalimide-tetrazine AIEgens,[99] expanding the utility of tetrazine-based AIEgens and showcasing the adaptability of this approach across different fluorophores (**5-2a–f**; Fig. 11, 12e and f). This cumulative work underscores the versatility of tetrazine-modified AIE systems and their potential for bioimaging and other fluorogenic applications.

To decipher the photophysical mechanism that drives the fluorogenic properties of tetrazine-based labels with aggregation-induced characteristics, Tang and co-workers conducted a detailed mechanistic analysis of these labels (**5-3a–c**; Fig. 11). Inspired by the "Matthew effect" from the psychosociological theory,[100] they adapted this concept to describe the photophysical processes unique to these labels (Scheme 4).[56]

Before the bio-orthogonal reactions, in the monomer form of **5-3c**, as with other tetrazine-integrated labels (Scheme 4a), a tetrazine-generated low-lying dark LE state is observed underneath the label-caused bright ICT state. Additional

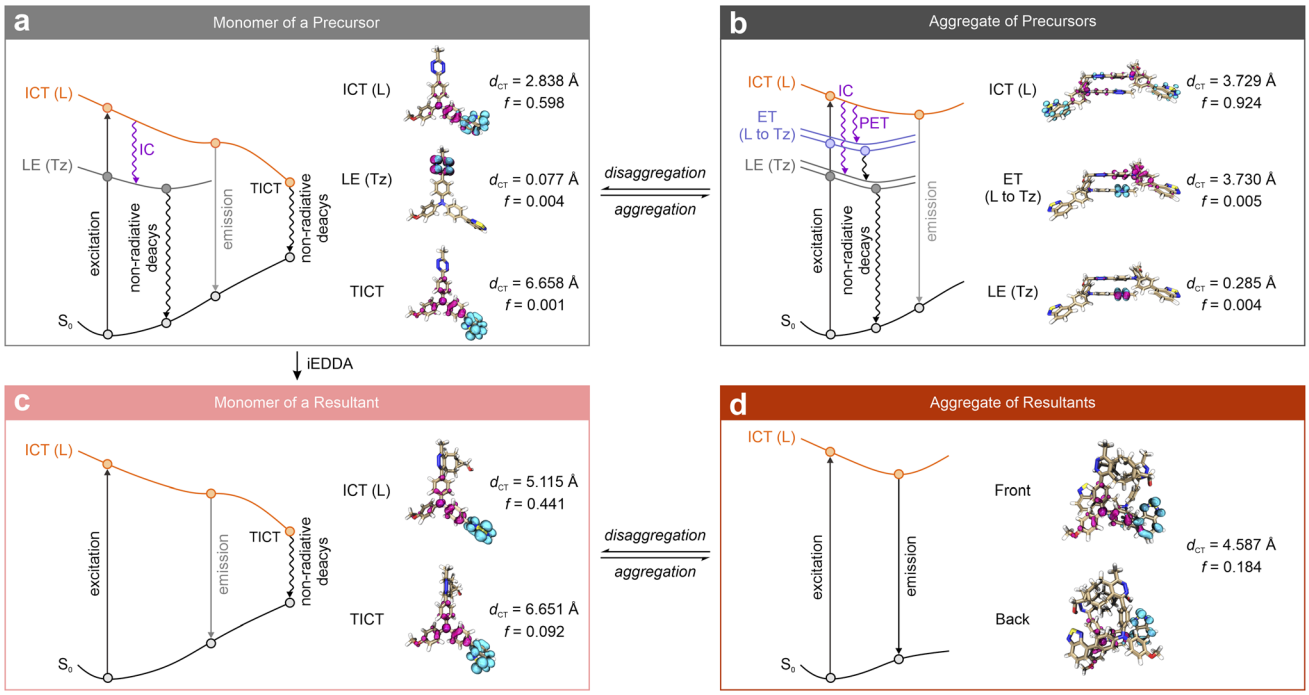

Scheme 4 Illustration of the "Matthew effect" in tetrazine labels represented by **5-3c** and its bio-orthogonal product triggered by BCN in the monomer and aggregate phases. Hole – highlighted in pink; electron – highlighted in cyan; L – entire label; Tz – tetrazine; S_0 – ground state; LE – locally excited; ICT – intramolecular charge transfer; TICT – twisted intramolecular charge transfer; IC – internal conversion; ET – electron transfer; PET – photoinduced electron transfer. Reproduced with permission from ref. 56. Copyright 2024, Wiley-VCH.

fluorescence quenching occurs due to the label's structural flexibility, which allows intramolecular rotations that bring the molecule into a twisted configuration, creating a twisted intramolecular charge transfer (TICT) state. Thus, the fluorescence of **5-3c** is synergistically quenched by multiple non-radiative decay channels, *i.e.*, IC and TICT, enhancing quenching efficiency prior to the iEDDA reactions. Even when the dye unintentionally binds to biomolecules and restricts intramolecular rotations, energy dissipation through IC can still minimize background emission.

Next, due to low solubility in water, most monomers of **5-3c** tend to aggregate prior to iEDDA reactions (Scheme 4b). In these aggregates, pairs of molecules form dimers with complex electronic states, including four dark states below the bright ICT state. The two lowest states, S_1 and S_2, are well-known LE states associated with n–π* transitions in the tetrazine fragments. Above these states, two additional dark ET states (S_3 and S_4) emerge due to interactions between neighboring molecules, displaying significantly larger d_{CT} values than S_1 and S_2. After photoexcitation, fluorescence in aggregated **5-3c** is suppressed through both IC within each monomer and PET between neighboring molecules. Thus, multiple dark states in aggregates synergistically enhance quenching, yielding extremely low background emissions. Notably, the dark ET states of S_3 and S_4 are specific to the aggregated form.

After undergoing iEDDA reactions, most tetrazine labels regain fluorescence as the reaction disrupts the tetrazine-induced dark LE state. Nonetheless, fluorescence recovery is limited in the BCN adduct of **5-3**. Despite the elimination of the tetrazine-caused dark LE state, the TICT state and other non-radiative decay channels, persisting due to intramolecular rotations, continue to quench fluorescence in the post-reacted label (Scheme 4c and Fig. S6, ESI†). In contrast, when aggregation occurs in the products, these intramolecular rotations are hindered by restricted free volume and reduced local polarity, which prevents the formation of the non-emissive TICT state (Scheme 4d). This aggregation thus triggers robust fluorescence activation, accompanied by dramatic FE responses.

Therefore, aggregation in tetrazine precursors provides additional quenching pathways *via* PET on top of tetrazine's intrinsic dark states, effectively reducing background emissions. Following bio-orthogonal reactions, aggregation enhances emission in the resulting fluorophores by inhibiting intramolecular rotations, markedly boosting FE values. The developed labels displayed unique aggregation-enhanced fluorogenic behaviors, *i.e.*, aggregation-caused quenching (ACQ) before bio-orthogonal reactions and AIE afterwards. This strategy advances the design, functionality, and versatility of tetrazine-based labels, paving the way for innovative bio-orthogonal imaging applications.

5.2 Torsion-induced disaggregation (TIDA) in tetrazine-isolated NIR labels

Pu and collaborators discovered a unique torsion-induced disaggregation (TIDA) phenomenon in NIR cyanine-tetrazine-based dyes (Fig. 13).[57] In these dyes, tetrazine does not act as a typical energy or electron acceptor. Instead, tetrazine ligation

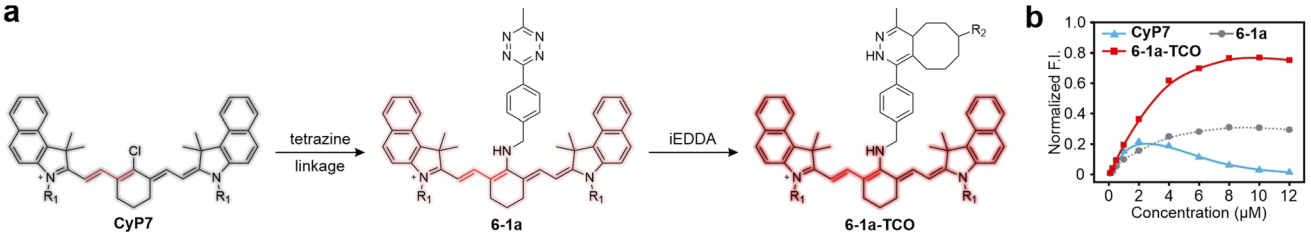

Fig. 13 (a) Structural variations associated with the TIDA process. Molecular structures of R1 and R2 are shown in Fig. S7, ESI.† (b) Concentration-dependence of peak F. I. of **CyP7**, **6-1a**, and **6-1a-TCO** in methanol. Reproduced with permission from ref. 57. Copyright 2022, Springer Nature.

and subsequent bio-orthogonal reactions enhance steric hindrance, promoting disaggregation and utilizing disaggregation-induced-emission to achieve the FE effect. In this configuration, tetrazine is linked to a cyanine fluorophore (**CyP7**), which exhibits NIR fluorescence and a small Stokes shift through a non-conjugated spacer. Owing to its flat configuration, **CyP7** exhibits a pronounced ACQ effect, as evidenced by the diminished peak fluorescence intensity with concentrations exceeding 2 μM (Fig. 13b). However, unlike conventional tetrazine-based dyes, attaching tetrazine to **CyP7** does not induce significant fluorescence quenching. This is because ETDS does not apply to NIR dyes, and the ΔE_L between tetrazine and **CyP7** is too large to activate effective PET quenching. In contrast, tetrazine attachment counteracts the inherent ACQ effect of **CyP7**. The fluorescence maximum of tetrazine-linked **CyP7** (**6-1a**) remains relatively constant even at higher concentrations (Fig. 13b), though some partial aggregation likely persists. Upon bio-orthogonal reaction with TCO derivatives, the increased steric hindrance further promotes disaggregation, leading to a 2.5-fold FE ratio at a dye concentration of 8 μM.

This remarkable TIDA effect broadens our understanding of tetrazine-based systems, challenging the perception of tetrazine solely as a fluorescence quencher. Although direct experimental data, such as crystal structures, are lacking to confirm *cis–trans* isomerization in the **CyP7** scaffold, it is convincing that bio-orthogonal reactions with tetrazine increase steric hindrance and promote disaggregation. This strategy may offer a pathway to convert many ACQ-prone fluorophores into fluorogenic systems.

6. Future directions

This section further proposes two design strategies to overcome the conventional wavelength limitations of tetrazine labels in the NIR spectrum by introducing additional novel quenching mechanisms to enable effective fluorogenicity. One approach involves linking tetrazine to a flexible NIR fluorophore (Scheme 5a). In the deep-red-to-NIR region, fluorescence quenching through the aforementioned energy flows or charge separation from the main fluorophore to tetrazine is generally restricted. However, rotatable bonds in the main fluorophore can induce a TICT state (or other dark states or conical intersection points), effectively quenching fluorescence in the monomeric phase. Following bio-orthogonal activations, the post-reacted labels would exhibit weak luminescence due to intramolecular rotations (Scheme 5b). As the reactions progress, the post-reacted labels accumulate, forming aggregated complexes (Scheme 5c). This aggregation restricts intramolecular rotations, thus deactivating the TICT quenching pathway and enabling strong fluorescence signals, *i.e.*, a favorable FE effect. Alternatively, bio-orthogonal reactions may anchor the labels to specific cellular locations, such as protein cavities or organelle membranes. Such binding could similarly restrict intramolecular rotations, restoring fluorescence and producing a marked FE effect.

An alternative strategy lies in attaching a quencher to a tetrazine-linked NIR fluorophore and designing a chemical reaction that specifically cleaves the quencher from the label.[101]

Initially, this quencher can substantially reduce the fluorescence of the tetrazine-conjugated fluorophore. Upon

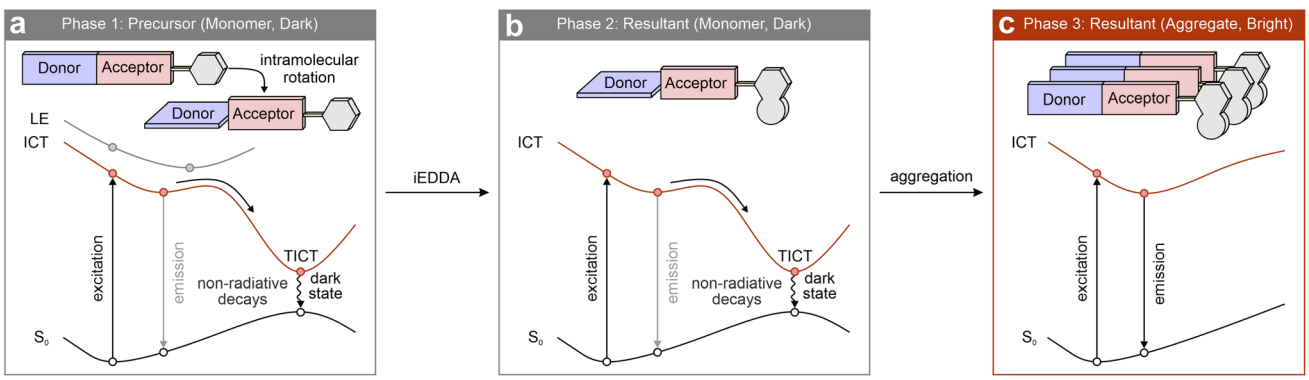

Scheme 5 Proposed design strategy and working mechanism. S_0 – ground state; ICT – intramolecular charge transfer; LE – locally excited; TICT – twisted intramolecular charge transfer.

cleavage of the quencher, the quenching pathway is interrupted, leading to a marked increment in fluorescence intensity. Simultaneously, the tetrazine group can interact bio-orthogonally with its counterparts to achieve targeted localization. This approach facilitates controlled and reaction-dependent fluorescence activation, making it ideal for applications that demand high specificity in fluorescence signaling.

In both strategies discussed, the tetrazine moiety functions primarily as a targeting agent rather than an energy or electron acceptor governing fluorogenicity. Specifically, the bio-orthogonal reactivity of tetrazine is employed to guide the label to the targeted location, while fluorescence is regulated through modulating intramolecular motions or cleaving the attached quencher. By decoupling the roles of bio-orthogonal targeting and fluorescence regulation, these methods also provide opportunities to integrate alternative quenching mechanisms into tetrazine labels, overcoming the traditional wavelength-dependent limitations in fluorogenicity.

7. Conclusions

Overall, this review comprehensively summarized the photophysical mechanisms of fluorogenicity in tetrazine-based fluorogenic labels, detailing label categorization by using connection modes and wavelengths. Within the visible spectrum, energy transfer (EnT) and internal conversion (IC) dominate quenching in tetrazine-isolated and tetrazine-integrated labels, respectively, while photoinduced charge separation processes, including photoinduced electron transfer (PET) and photoinduced charge centralization (PCC), become central in the deep-red and NIR regions. The review also highlights how molecular aggregation/disaggregation phenomena, such as the "Matthew effect" and torsion-induced disaggregation (TIDA), can modulate fluorogenic properties. Looking ahead, the review suggests advancing the fluorogenic behaviors of tetrazine labels by optimizing intramolecular rotations and integrating alternative quenching mechanisms to achieve NIR fluorogenicity without compromising bio-orthogonal functionality. These photophysical insights aim to inspire research into next-generation tetrazine-functionalized labels with enhanced fluorogenic properties, paving the way for expanded applications in bio-orthogonal contexts.

Data availability

No primary research results, software, or code have been included, and no new data were generated or analyzed as part of this review.

Author contributions

T. S.: conceptualization, methodology, investigation, formal analysis, visualization, writing – original draft, and writing – review & editing; X. L.: software, project administration, supervision, funding acquisition, resources, data curation, and writing – review & editing.

Conflicts of interest

There are no conflicts to declare.

Acknowledgements

This work was supported by the Singapore University of Technology and Design (SUTD; SKI 2021_04_09). T. S. acknowledges the scholarship support from the Doctor of Philosophy program at SUTD.

Notes and references

1 N. K. Devaraj and R. Weissleder, *Acc. Chem. Res.*, 2011, **44**, 816–827.
2 H. Wu and N. K. Devaraj, *Acc. Chem. Res.*, 2018, **51**, 1249–1259.
3 J. Mondal and A. Sivaramakrishna, *Top. Curr. Chem.*, 2022, **380**, 34.
4 N. K. Devaraj, R. Weissleder and S. A. Hilderbrand, *Bioconjugate Chem.*, 2008, **19**, 2297–2299.
5 R. E. Bird, S. A. Lemmel, X. Yu and Q. A. Zhou, *Bioconjugate Chem.*, 2021, **32**, 2457–2479.
6 G. N. Lipunova, E. V. Nosova, G. V. Zyryanov, V. N. Charushin and O. N. Chupakhin, *Org. Chem. Front.*, 2021, **8**, 5182–5205.
7 A. Darko, S. Wallace, O. Dmitrenko, M. M. Machovina, R. A. Mehl, J. W. Chin and J. M. Fox, *Chem. Sci.*, 2014, **5**, 3770–3776.
8 M. L. Blackman, M. Royzen and J. M. Fox, *J. Am. Chem. Soc.*, 2008, **130**, 13518–13519.
9 E. M. Sletten and C. R. Bertozzi, *Acc. Chem. Res.*, 2011, **44**, 666–676.
10 J. Šečkutė and N. K. Devaraj, *Curr. Opin. Chem. Biol.*, 2013, **17**, 761–767.
11 Y. Chen, H. Jiang, T. Hao, N. Zhang, M. Li, X. Wang, X. Wang, W. Wei and J. Zhao, *Chem. Biomed. Imaging*, 2023, **1**, 590–619.
12 J. Yang, B. Zhu and C. Ran, *Chem. Biomed. Imaging*, 2023, **1**, 434–447.
13 Y. Liao, Y. Liang, Y. Huang, X. Zeng, T. He and J. Yin, *Chin. Chem. Lett.*, 2024, **35**, 109092.
14 E. Kozma and P. Kele, *Top. Curr. Chem.*, 2024, **382**, 7.
15 Kenry and B. Liu, *Trends Chem.*, 2019, **1**, 763–778.
16 M. C. Giel and Y. Hong, *Aggregate*, 2023, **4**, e336.
17 Q. Min and X. Ji, *J. Med. Chem.*, 2023, **66**, 16546–16567.
18 Y. Wang, C. Zhang, H. Wu and P. Feng, *Molecules*, 2020, **25**, 5640.
19 R. Pareja Tello, S. Wang, F. Fontana, A. Correia, G. Molinaro, S. Lopez Cerda, S. Hietala, J. Hirvonen, G. Barreto and H. A. Santos, *Biomater. Sci.*, 2023, **11**, 4972–4984.
20 X. Ji, Z. Pan, B. Yu, L. K. De La Cruz, Y. Zheng, B. Ke and B. Wang, *Chem. Soc. Rev.*, 2019, **48**, 1077–1094.
21 R. M. Versteegen, R. Rossin, W. ten Hoeve, H. M. Janssen and M. S. Robillard, *Angew. Chem., Int. Ed.*, 2013, **52**, 14112–14116.

22 L. Zhou, Z. Wang, L. Wang, X. Zhang and Y. Xiao, *J. Am. Chem. Soc.*, 2023, **145**, 28296–28306.
23 E. G. Tomarchio, R. Turnaturi, E. Saccullo, V. Patamia, G. Floresta, C. Zagni and A. Rescifina, *Bioorg. Chem.*, 2024, **150**, 107573.
24 Z. Li, Q. Chen, J. Wang, X. Pan and W. Lu, *Top. Curr. Chem.*, 2021, **379**, 39.
25 X. Xie, B. Li, J. Wang, C. Zhan, Y. Huang, F. Zeng and S. Wu, *ACS Appl. Mater. Interfaces*, 2019, **11**, 41875–41888.
26 T. He, C. Ren, Y. Luo, Q. Wang, J. Li, X. Lin, C. Ye, W. Hu and J. Zhang, *Chem. Sci.*, 2019, **10**, 4163–4168.
27 Z. Tan, M. Lin, J. Liu, H. Wu and H. Chao, *Dalton Trans.*, 2024, **53**, 12917–12926.
28 J. Huang, Z. Yao, B. Li and Y. Ping, *J. Controlled Release*, 2023, **361**, 270–279.
29 J. Wu, T. Sun, C. Yang, T. Lv, Y. Bi, Y. Xu, Y. Ling, J. Zhao, R. Cong, Y. Zhang, J. Wang, H. Wen, H. Jiang, F. Li and Z. Huang, *Biomater. Sci.*, 2021, **9**, 1816–1825.
30 L. K. B. Tam and D. K. P. Ng, *Mater. Chem. Front.*, 2023, **7**, 3184–3193.
31 I. Ortiz-Gomez, M. Ortega-Munoz, A. Salinas-Castillo, J. A. Alvarez-Bermejo, M. Ariza-Avidad, I. de Orbe-Paya, F. Santoyo-Gonzalez and L. F. Capitan-Vallvey, *Talanta*, 2016, **160**, 721–728.
32 T. W. Myers, C. J. Snyder, D. E. Chavez, R. J. Scharff and J. M. Veauthier, *Chem. - Eur. J.*, 2016, **22**, 10590–10596.
33 Z. Zhao, L. Cao, T. Zhang, R. Hu, S. Wang, S. Li, Y. Li and G. Yang, *ChemistrySelect*, 2016, **1**, 2581–2585.
34 A.-C. Knall and C. Slugovc, *Chem. Soc. Rev.*, 2013, **42**, 5131–5142.
35 S. Mayer and K. Lang, *Synthesis*, 2017, **49**, 830–848.
36 K. Kang, J. Park and E. Kim, *Proteome Sci.*, 2016, **15**, 1–13.
37 J. Tu, M. Xu, S. Parvez, R. T. Peterson and R. M. Franzini, *J. Am. Chem. Soc.*, 2018, **140**, 8410–8414.
38 H. Stockmann, A. A. Neves, S. Stairs, K. M. Brindle and F. J. Leeper, *Org. Biomol. Chem.*, 2011, **9**, 7303–7305.
39 J. Tu, D. Svatunek, S. Parvez, H. J. Eckvahl, M. Xu, R. T. Peterson, K. N. Houk and R. M. Franzini, *Chem. Sci.*, 2020, **11**, 169–179.
40 X. Jiang, M. Li, Y. Wang, C. Wang, Y. Wang, T. Shen, L. Shen, X. Liu, Y. Wang and X. Li, *Nat. Commun.*, 2023, **14**, 1401.
41 A. Loredo, J. Tang, L. Wang, K. L. Wu, Z. Peng and H. Xiao, *Chem. Sci.*, 2020, **11**, 4410–4415.
42 R. Zhang, Y. Teng, G. Shao, Y. Wang, H. Yang and Y. Tian, *Mater. Chem. Front.*, 2024, **8**, 2341–2349.
43 C. Wang, C. Liu, Q. Wei, L. Yang, P. Yang, Y. Li and Y. Cheng, *Research*, 2020, 6563091.
44 H. Sun, Q. Xue, C. Zhang, H. Wu and P. Feng, *Org. Chem. Front.*, 2022, **9**, 481–498.
45 A. Hamsath, O. L. Lederberg, Q. Cui, M. Shieh, Y. Lam, B. J. Brummett, S. Xu, J. R. Robinson and M. Xian, *Chem. Sci.*, 2022, **13**, 10336–10341.
46 R. Garcia-Vazquez, U. M. Battisti, J. T. Jorgensen, V. Shalgunov, L. Hvass, D. L. Stares, I. N. Petersen, F. Crestey, A. Loffler, D. Svatunek, J. L. Kristensen, H. Mikula, A. Kjaer and M. M. Herth, *Chem. Sci.*, 2021, **12**, 11668–11675.
47 A. Wieczorek, P. Werther, J. Euchner and R. Wombacher, *Chem. Sci.*, 2017, **8**, 1506–1510.
48 S. Segawa, X. He and B. Z. Tang, *Luminescence*, 2024, **39**, e4619.
49 X. Chen and Y.-W. Wu, *Org. Biomol. Chem.*, 2016, **14**, 5417–5439.
50 H. Son, D. Kim, S. Kim, W. G. Byun and S. B. Park, *Angew. Chem., Int. Ed.*, 2024, e202421982, DOI: **10.1002/anie.202421982**.
51 B. Pinto-Pacheco, W. P. Carbery, S. Khan, D. B. Turner and D. Buccella, *Angew. Chem., Int. Ed.*, 2020, **59**, 22140–22149.
52 W. Chi, L. Huang, C. Wang, D. Tan, Z. Xu and X. Liu, *Mater. Chem. Front.*, 2021, **5**, 7012–7021.
53 T. Shen, W. Zhang, P. Yadav, X. W. Sun and X. Liu, *Mater. Chem. Front.*, 2023, **7**, 1082–1092.
54 T. Shen, X. Li and X. Liu, *Mater. Chem. Front.*, 2024, **8**, 2135–2141.
55 T. Shen and X. Liu, *Bioconjugate Chem.*, 2024, **35**, 1024–1032.
56 S. Segawa, X. Ou, T. Shen, T. Ryu, Y. Ishii, H. H. Y. Sung, I. D. Williams, R. T. K. Kwok, K. Onda, K. Miyata, X. He, X. Liu and B. Z. Tang, *Aggregate*, 2024, **5**, e499.
57 X. Zhang, J. Gao, Y. Tang, J. Yu, S. S. Liew, C. Qiao, Y. Cao, G. Liu, H. Fan, Y. Xia, J. Tian, K. Pu and Z. Wang, *Nat. Commun.*, 2022, **13**, 3513.
58 N. K. Devaraj, S. Hilderbrand, R. Upadhyay, R. Mazitschek and R. Weissleder, *Angew. Chem., Int. Ed.*, 2010, **49**, 2869–2872.
59 J. C. Carlson, L. G. Meimetis, S. A. Hilderbrand and R. Weissleder, *Angew. Chem., Int. Ed.*, 2013, **52**, 6917–6920.
60 P. Werther, K. Yserentant, F. Braun, K. Grussmayer, V. Navikas, M. Yu, Z. Zhang, M. J. Ziegler, C. Mayer, A. J. Gralak, M. Busch, W. Chi, F. Rominger, A. Radenovic, X. Liu, E. A. Lemke, T. Buckup, D. P. Herten and R. Wombacher, *ACS Cent. Sci.*, 2021, **7**, 1561–1571.
61 M. Vrabel, P. Kolle, K. M. Brunner, M. J. Gattner, V. Lopez-Carrillo, R. de Vivie-Riedle and T. Carell, *Chem. - Eur. J.*, 2013, **19**, 13309–13312.
62 A. Vazquez, R. Dzijak, M. Dracinsky, R. Rampmaier, S. J. Siegl and M. Vrabel, *Angew. Chem., Int. Ed.*, 2017, **56**, 1334–1337.
63 S. J. Siegl, A. Vazquez, R. Dzijak, M. Dracinsky, J. Galeta, R. Rampmaier, B. Klepetarova and M. Vrabel, *Chem. - Eur. J.*, 2018, **24**, 2426–2432.
64 S. J. Siegl, J. Galeta, R. Dzijak, A. Vázquez, M. Del Río-Villanueva, M. Dračínský and M. Vrabel, *ChemBioChem*, 2019, **20**, 886–890.
65 S. J. Siegl, J. Galeta, R. Dzijak, M. Dracinsky and M. Vrabel, *ChemPlusChem*, 2019, **84**, 493–497.
66 Y. Lee, W. Cho, J. Sung, E. Kim and S. B. Park, *J. Am. Chem. Soc.*, 2018, **140**, 974–983.
67 H. Wu, J. Yang, J. Seckute and N. K. Devaraj, *Angew. Chem., Int. Ed.*, 2014, **53**, 5805–5809.

68 G. Linden, L. Zhang, F. Pieck, U. Linne, D. Kosenkov, R. Tonner and O. Vazquez, *Angew. Chem., Int. Ed.*, 2019, **58**, 12868–12873.
69 M. Işık and M. A. Kisaçam, *J. Org. Chem.*, 2024, **89**, 6513–6519.
70 H. Wu, B. T. Cisneros, C. M. Cole and N. K. Devaraj, *J. Am. Chem. Soc.*, 2014, **136**, 17942–17945.
71 J. Šečkutė, J. Yang and N. K. Devaraj, *Nucleic Acids Res.*, 2013, **41**, e148.
72 P. Werther, J. S. Mohler and R. Wombacher, *Chem. - Eur. J.*, 2017, **23**, 18216–18224.
73 L. G. Meimetis, J. C. Carlson, R. J. Giedt, R. H. Kohler and R. Weissleder, *Angew. Chem., Int. Ed.*, 2014, **53**, 7531–7534.
74 J. Galeta, R. Dzijak, J. Oboril, M. Dracinsky and M. Vrabel, *Chem. - Eur. J.*, 2020, **26**, 9945–9953.
75 D. Kim, J. H. Lee, J. Y. Koo, H. M. Kim and S. B. Park, *Bioconjugate Chem.*, 2020, **31**, 1545–1550.
76 M. E. Graziotto, L. D. Adair, A. Kaur, P. Verite, S. R. Ball, M. Sunde, D. Jacquemin and E. J. New, *RSC Chem. Biol.*, 2021, **2**, 1491–1498.
77 E. Albitz, K. Nemeth, G. Knorr and P. Kele, *Org. Biomol. Chem.*, 2023, **21**, 7358–7366.
78 L. K. B. Tam, P. C. Lo, P. C. K. Cheung and D. K. P. Ng, *Chem. - Asian J.*, 2023, **18**, e202300562.
79 S. K. Choi, J. Kim and E. Kim, *Molecules*, 2021, **26**, 1868.
80 T. Forster, *Naturwissenschaften*, 1946, **33**, 166–175.
81 D. L. Dexter, *J. Chem. Phys.*, 1953, **21**, 836–850.
82 S. Speiser, *Chem. Rev.*, 1996, **96**, 1953–1976.
83 J. Fan, M. Hu, P. Zhan and X. Peng, *Chem. Soc. Rev.*, 2013, **42**, 29–43.
84 G. Beliu, A. J. Kurz, A. C. Kuhlemann, L. Behringer-Pliess, M. Meub, N. Wolf, J. Seibel, Z. D. Shi, M. Schnermann, J. B. Grimm, L. D. Lavis, S. Doose and M. Sauer, *Commun. Biol.*, 2019, **2**, 261.
85 M. Bojtar, K. Nemeth, F. Domahidy, G. Knorr, A. Verkman, M. Kallay and P. Kele, *J. Am. Chem. Soc.*, 2020, **142**, 15164–15171.
86 S.-K. Choi, Y. Lee, S. E. Yoon, H. Choi, J. Kim, J. H. Kim, S. Lee, W. Kim and E. Kim, *Sens. Actuators, B*, 2021, **340**, 129966.
87 W. Mao, J. Tang, L. Dai, X. He, J. Li, L. Cai, P. Liao, R. Jiang, J. Zhou and H. Wu, *Angew. Chem., Int. Ed.*, 2021, **60**, 2393–2397.
88 M. O. Loehr and N. W. Luedtke, *Angew. Chem., Int. Ed.*, 2022, **61**, e202112931.
89 D. Kim, H. Son and S. B. Park, *Angew. Chem., Int. Ed.*, 2023, **62**, e202310665.
90 P. Geng, E. List, F. Ronicke and H. A. Wagenknecht, *Chem. - Eur. J.*, 2023, **29**, e202203156.
91 B. Pfeuffer, P. Geng and H. A. Wagenknecht, *ChemBioChem*, 2024, **25**, e202300739.
92 T. Shen, Y. Gao, C. Wang, Z. Xu and X. Liu, *J. Phys. Chem. B*, 2021, **125**, 1447–1452.
93 L. Chen, F. Li, M. Nandi, L. Huang, Z. Chen, J. Wei, W. Chi, X. Liu and J. Yang, *Dyes Pigm.*, 2020, **177**, 108313.
94 W. Mao, W. Chi, X. He, C. Wang, X. Wang, H. Yang, X. Liu and H. Wu, *Angew. Chem., Int. Ed.*, 2022, **61**, e202117386.
95 D. Wu and D. F. O'Shea, *Chem. Commun.*, 2017, **53**, 10804–10807.
96 L. Chen, F. Li, Y. Li, J. Yang, Y. Li and B. He, *Chem. Commun.*, 2022, **58**, 298–301.
97 Z. He, T. Ishizuka, Y. Hishikawa and Y. Xu, *Chem. Commun.*, 2022, **58**, 12479–12482.
98 Y. Teng, R. Zhang, B. Yang, H. Yang, X. Li, D. Yin, X. Feng and Y. Tian, *J. Mater. Chem. B*, 2022, **10**, 8642–8649.
99 Y. Wang, Y. Teng, H. Yang, X. Li, D. Yin and Y. Tian, *Chem. Commun.*, 2022, **58**, 949–952.
100 R. K. Merton, *Science*, 1968, **159**, 56–63.
101 Y. Wang, D. Torres-García, T. P. Mostert, L. Reinalda and S. I. Van Kasteren, *Angew. Chem., Int. Ed.*, 2024, **63**, e202401733.